*Review*

# Graphene Quantum Dot-Enabled Nanocomposites as Luminescence- and Surface-Enhanced Raman Scattering Biosensors

Darwin Kurniawan [ID], Yan-Yi Chen [ID], Neha Sharma, Michael Ryan Rahardja and Wei-Hung Chiang *[ID]

Department of Chemical Engineering, National Taiwan University of Science and Technology, Taipei 10607, Taiwan
* Correspondence: whchiang@mail.ntust.edu.tw

**Abstract:** Graphene quantum dots (GQDs) are a zero-dimensional (0D) carbon-based nanomaterial with a unique quantum confinement effect that have captured the eyes of many researchers. In addition to their luminescence properties, a high biocompatibility and large surface area have enabled GQDs to be used for many applications, and even be integrated with either organic or inorganic materials to produce GQD nanocomposites to enhance the application performances and broaden the application scope. In this review, we aim to highlight the exquisite properties and synthesis methods of GQDs, recent advances in the fabrication of GQD nanocomposites with both organic and inorganic materials, and their corresponding luminescence-based and surface enhanced Raman scattering (SERS)-based biosensing applications. Finally, this review article concludes with a summary of current challenges and prospects.

**Keywords:** graphene quantum dots; nanocomposites; luminescence; surface enhanced Raman scattering; biosensing

## 1. Introduction

Owing to the currently escalating issue of energy limitation, much interest and effort has been focused on the utilization of carbon-based nanomaterials for advanced applications. The rise of carbon-based nanomaterials was pioneered from the discovery of buckminsterfullerene by Kroto et al. in 1985 [1], which further evolved into other discoveries of carbon nanotubes (CNTs) by Iijima in 1991 [2] and graphene by Novoselov et al. in 2004 [3]. Since graphene is a two-dimensional (2D) material composed of long-conjugated $sp^2$ carbon in a honeycomb network, it can exhibit outstanding electron mobility due to the quantum Hall effect [4]. Interestingly, the spatial confinement of 2D graphene down to the 0D scale of approximately <100 nm causes bandgap opening, leading to the new quantum confinement and edge effect phenomena [5]. This newly discovered material was called graphene quantum dots (GQDs) and has been used at the forefront of vast research interest due to its unique and tunable luminescence properties [6,7]. Due to their high photo- and chemical-stability, biocompatibility, large surface area and low toxicity, GQDs have been widely used for optical-based sensing [8–10], imaging [11,12], drug delivery [13], catalysis [14] and even optoelectronic- and energy-related applications [15–18], similar to perovskite QDs [19,20].

To further improve their application performance and practicality, GQDs can be integrated with either organic or inorganic materials to yield multifunctional nanocomposites. Polymeric matrices are the most commonly used organic materials to host GQDs, in which GQDs can not only provide luminescence response to external stimuli, but also act as nanocross-linkers to enhance the mechanical properties of the nanocomposite due to the establishment of either covalent or non-covalent interactions between the surface functional groups and side chains of the GQD and polymer, respectively [21]. On the other hand,

inorganic materials, particularly plasmonic nanoparticles, have been the first choice for surface-enhanced Raman scattering (SERS) applications owing to the generation of an electromagnetic mechanism (EM) [22]. The combination of GQDs with plasmonic nanoparticles can offer an additional chemical mechanism (CM) to increase the enhanced factor (EF) of SERS applications and improve biomolecule adsorption via π–π interaction, making this nanocomposite suitable for use as a SERS-based biosensor.

This review will focus on the properties and synthesis of GQDs and their nanocomposites with various organic and inorganic materials for luminescence- and SERS-based biosensing applications (Figure 1). We will comprehensively review the most exquisite properties of GQDs (Section 2), the synthetic methods of GQDs complemented with the currently thriving sustainable synthesis from natural resources (Section 3), the fabrication of GQD nanocomposites with organic and inorganic materials (Section 4) and the luminescence- and SERS-based biosensing applications of GQD nanocomposites in Sections 5 and 6, respectively. Finally, this review will be concluded in Section 7 with a summary and perspectives regarding the current challenges for GQD nanocomposites in biosensing applications.
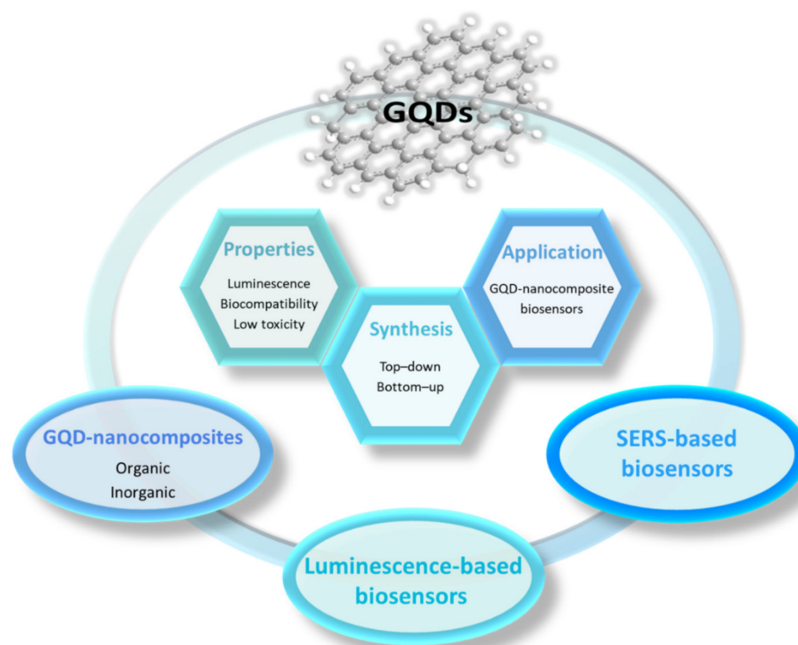


**Figure 1.** Overview of the main topics about GQD nanocomposites discussed in this review.

## 2. Properties of GQDs

GQDs possess a graphitic lattice as the core with zig-zag and/or armchair edges, while the distinction between GQDs and the other 0D-carbon nanomaterials, such as carbon dots (CDs) and carbon quantum dots (CQDs), sometimes still appears quite unclear. One of the most straightforward methods of distinguishing those 0D nanomaterials is to investigate their morphological structures via high-resolution transmission electron microscopy (HR-TEM). GQDs are hybridized by long-conjugated sp$^2$ carbon [5], while CDs and CQDs are comprised of fully amorphous and a combination of crystalline and amorphous carbon [16], respectively. Therefore, a clear lattice structure of GQDs can be observed from the HR-TEM image and their X-ray diffraction (XRD) peak will appear to be relatively sharper than those of CDs and CQDs [23].

GQDs possess a strong UV absorption peak at approximately 200–330 nm and absorption shoulder or tail at approximately 270–390 nm, which can be ascribed to the π–* transition of the sp$^2$ carbon core and the n–π* transition of oxygen-containing functional groups [24,25], respectively. The most notable optical properties of GQDs are their luminescence, due to quantum confinement and edge effects, as well as emissive traps. The origin

of the luminescence of GQDs is almost similar to that of CQDs, but not that of CDs, which is related to the absence of quantum confinement. Despite the discovery of a quantum confinement effect in GQDs by Ponomarenko et al. in 2008 [5], the luminescence of GQDs was reported by Pan et al. two years later [6]. Afterwards, many efforts have been employed to reveal the luminescence mechanism, yet it still remains unclear. The difficulties mostly lie in the inhomogeneity of the materials resulting from different synthetic methods or even from the same method [25].

Nonetheless, the general luminescence mechanism can be explained by the radiative electron-hole recombination upon electron excitation by an external energy source [26]. There are three possible energy sources that can be used to excite the electron from the highest occupied molecular orbital (HOMO) to the lowest unoccupied molecular orbital (LUMO) of GQDs: photon (photoluminescence; PL), chemical (chemiluminescence; CL) and electrochemical (electrochemiluminescence; ECL). Compared with CL and ECL, more fundamental and application studies about PL have been reported so far. In addition, the emissions of GQDs are tunable by modifying their bandgap through size control (Figure 2a) [7,27], surface functionalization (Figure 2b) [28] and doping with heteroatoms (Figure 2c) [7,29]. For example, nitrogen-doped GQDs (NGQDs) can be synthesized by (1) treating the synthesized GQDs with N-containing precursors, such as hydrazine [30], at a high temperature and long reaction time; (2) using C- and N-containing molecules, such as chitosan [31], melamine [32] and a mixture of citric acid with urea [33] or graphene oxide with ammonia [34], as the precursors of NGQDs. The synthesis of GQDs will be discussed more in a latter section, while a more detailed discussion of the heteroatom-doped GQDs can be seen in other reviews [9,35]. In addition to altering the bandgap, the integration of heteroatoms into the carbon core of GQDs can also increase the luminescence quantum yield and introduce new properties to the GQDs [35]. This doping strategy is also often applied to both CDs and CQDs to improve their functionalities [36].
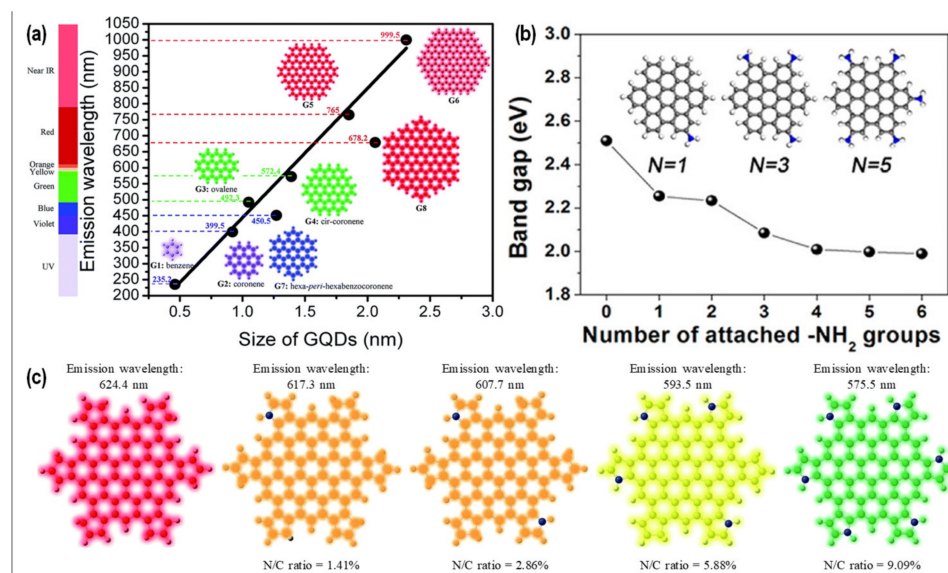


**Figure 2.** Tunable-emission GQDs induced with bandgap alteration. Emission-controlled GQDs via (**a**) size modification [7], (**b**) surface functionalization [28], and (**c**) heteroatom doping [7].

Another attractive property of GQDs is biocompatibility, which can be defined as the capability of a material to be implemented in particular applications without showing any tissue or cell cytotoxicity. Therefore, GQDs are more suitable to be utilized in biological-related applications (in vitro and in vivo) compared with conventional metallic semiconductor QDs and higher-dimensional (1D and 2D) carbon nanomaterials such as CNT and graphene oxide [37–41]. Notably, some studies reported that GQDs can still cause cell death due to the generation of intracellular reactive oxygen species. Therefore,

according to the review article by Wang et. al. [39], the cytotoxicity of GQDs depends on their dosage concentration, synthesis method, size, surface chemistry and doping.

## 3. Synthesis of GQDs

There are two basic GQD-synthesis approaches, including top–down and bottom–up approaches. In the top–down approach, higher-dimensional carbon materials, such as coal [42,43], coke [44], graphite [45], graphene [6], CNT [46,47] and carbon fiber (CF) [48], are exfoliated by means of a chemical, mechanical or electrochemical method to produce GQDs. This approach can offer large-scale production and high crystallinity owing to the inheritance of a highly graphitic nature from the precursor, but the use of non-renewable precursors, strong acids and toxic-chemical-reducing agents coupled with the high temperature and long reaction time required are major drawbacks. In addition, it is also challenging to achieve GQD synthesis with well-controlled structures and properties, limiting the feasibility and possibility of GQDs for a broad application scope. Meanwhile, the bottom–up approach involves the production of GQDs from pyrolysis, carbonization or a chemical reaction of small organic molecules or aromatic hydrocarbons. This bottom–up approach can offer GQD synthesis with controlled-structures and properties, as well as addressing the current energy limitation issue by utilizing earth-bound natural resources as the main precursors for GQDs synthesis. More detailed discussion about GQDs synthesis will be provided below.

### 3.1. Top–Down Approach

Figure 3a shows the GQD synthesis process from coal using the chemical exfoliation method. In the typical procedure, a mixture of coal and concentrated sulfuric acid and nitric acid, with a volume ratio of 3:1, is sonicated for 2 h, followed by heating in an oil bath at 100 or 120 °C with continuous stirring for 24 h [42]. The production yields were in the range of 10–20 wt%. By changing the exfoliation temperature from 100 to 120 °C, both the particle size and the PL emission could be tuned from ~2.3 to ~2.9 nm and 460 to 500 nm, respectively. Owing to the disordered configuration and small crystalline domains, coal offers more advantages as GQDs precursors than graphite, including the ease of dispersion, exfoliation, functionalization and chemical cutting. Therefore, milder oxidative reaction conditions can be applied for coal but not for graphite. Treating coal at a high temperature of up to 1000 °C leads to an enlargement in the aromatic domain and improvement in the $sp^2$ carbon content. As a consequence, not only is the electrical conductivity significantly improved, but coke can also serve as a good candidate for the synthesis of GQDs using the electrochemical method. He et al. reported the electrochemical synthesis of tunable-emission GQDs from coke by regulating the applied current density and the electrolyte mixture ratio (Figure 3b) [44]. The emissions of GQDs could be tuned to shorter wavelengths (560 to 500 nm; orange to green) by increasing the applied current density and water to methanol ratio to the electrolyte. Blue-emission GQDs were obtained through a chemical reduction of green-emission GQDs for 4 h, with $NaBH_4$ as the reducing agent. The average particle sizes of the synthesized GQDs were also found to decrease from 4.6 to 2.9 nm for orange-to-blue-emission GQDs.

Since GQDs are graphene derivatives, GQDs can also be prepared from graphene sheets. In 2010, Pan et al. were the first to report the luminescence properties of GQDs, in which graphene as the precursor was used and hydrothermally cut into GQDs at 200 °C for 10 h (Figure 3c) [6]. The synthesized GQDs exhibited excitation-dependent behavior, with the strongest emissions at 430 nm under 320 nm excitation with a PLQY of 6.9% relative to quinine sulfate (QS). On the other hand, 1D-carbon nanomaterials can also be used to synthesize GQDs. Shinde et al. utilized an electrochemical method to oxidize and reduce multi-walled CNTs into GQDs (Figure 3d) [46]. Different sizes of GQDs, including 8.2 ± 0.3, 5 ± 0.3 and 3 ± 0.3 nm, were obtained through an electrochemical reaction at 90 °C for 7, 11, and 15 h, respectively. Peng et al. utilized a chemical oxidation method to cut CFs into a mixture of concentrated sulfuric acid and nitric acid under 80–120 °C for 24 h to

obtain GQDs with different sizes (Figure 3e) [48]. As the reaction temperature decreased from 120 to 80 °C, the GQD size increased from 3 to 9 nm and the corresponding emission wavelength shifted from 434 to 564 nm.
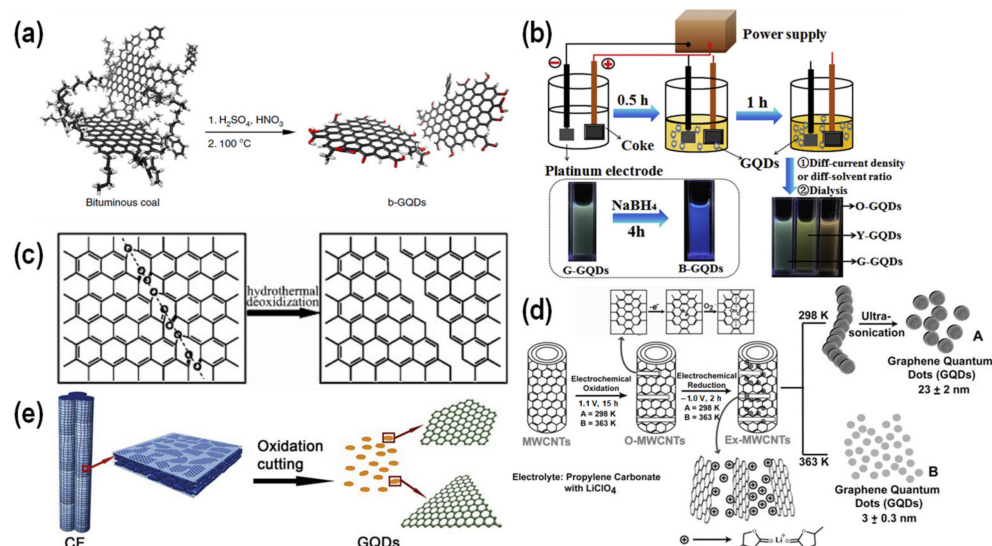


**Figure 3.** Synthesis of GQDs based on top–down approach. GQDs synthesis from (**a**) coal [42], (**b**) coke [44], (**c**) graphene [6], (**d**) CNT [46] and (**e**) carbon fiber [48].

### 3.2. Bottom–Up Approach

In the bottom–up approach, small organic or aromatic hydrocarbon molecules are often used as the main carbon source for the synthesis of GQDs. Since aromatic hydrocarbon molecules are stable, high temperatures up to >600 °C are required to initiate hydrogen elimination and graphitization under catalyst-free conditions. However, Wang et al. were able to reduce the reaction temperature to 90–200 °C for the hydrothermal fusion of pyrene into GQDs under alkaline conditions [49]. In the typical procedure, pyrene was first nitrated into trinitropyrene in nitric acid at 80 °C for 12 h. Afterwards, the obtained trinitropyrene was dispersed in 0.2 M NaOH solution and further subjected to hydrothermal treatment at 200 °C for 10 h. The presence of three positively charged $NO_2$ groups in trinitropyrene enabled a nucleophilic substitution with many alkaline species, enhancing the reactivity of trinitropyrene for the synthesis of OH-functionalized GQDs (OH-GQDs), with an overall production yield of 63%. The resulting OH-GQDs were $3.5 \pm 0.6$ nm and displayed strong green emissions under 365 nm UV irradiation with a PLQY of 23% relative to Rhodamine 6G. Additionally, the synthesis procedure could also be applied to the synthesis of amine-functionalized GQDs (amine-GQDs) by adding ammonia and hydrazine to the hydrothermal step, yielding GQDs with different emissions, including blue, cyan and yellow. This trinitropyrene can also be fused with thiourea in a mixture of NaOH and *N,N*-dimethylformamide (DMF) under a hydrothermal process at 200 °C for 10 h to produce nitrogen and sulfur co-doped GQDs (N,S-GQDs), with a high production yield and absolute PLQY of 87.8 and 23.2%, respectively [50].

Syntheses of GQDs from natural resources have recently been one of the major interests to increase sustainability and address the energy limitation issue [51]. Moreover, the use of natural resources is also considered to be more environmentally friendly than aromatic hydrocarbons. Blue-luminescent GQDs with excitation-independent emissions that were at their strongest intensity at 460 nm under 362 nm excitation were synthesized from the pyrolysis of citric acid at 200 °C for 30 min [52]. Dong et al. attributed the conversion of citric acid into GQDs to the incomplete carbonization of citric acid, while complete carbonization of citric acid resulted in the formation of graphene oxide [52], as shown in Figure 4a. Tang et al. utilized a microwave-assisted hydrothermal method to convert glucose into GQDs (Figure 4b) [53]. It was found that the microwave power, heating

time, precursor concentration and solution volume could influence the growth of GQDs differently. For a particular parameter, blue-emission GQDs, with an average particle size of 3.4 ± 0.5 nm and an absolute PLQY of 11%, were obtained when 11.1 wt% of glucose was subjected to a 595 W microwave treatment for 5 min.

Recently, biomass has attracted attention for the synthesis of GQDs in a more sustainable way [51]. Despite being the most abundant natural aromatic on Earth, lignin is regarded as a waste product in the pulping industry. A study conducted by Ding et al. revealed the possibility of producing GQDs from alkali lignin using a two-step fabrication method, which is depicted in Figure 4c [54]. The first step involved the generation of lignin segments through the oxidized cleavage of the β-O-4 ether linkage of the lignin structure in concentrated nitric acid for 12 h. In the second step, these formed segments, which contained both oxygen- and nitrogen-functional groups, were refused into NGQDs using a hydrothermal treatment at 180 °C for 12 h. The produced NGQDs were approximately 3.7 nm, exhibiting an excitation-dependent emission that peaked at 410 nm under 310 nm excitation. Both the production yield and PLQY were estimated to be around 21%. On the other hand, chitosan, one of the most abundant compounds on Earth, can also be used for the synthesis of GQDs. An early study reported by Kumar et al. produced NGQDs from chitosan in using one-step synthesis via a chemical vapor deposition (CVD) method at 250–300 °C [55]. The size of the NGQDs could be tailored by controlling the growth process time, where 3 min of growth process produced 10–15 nm NGQDs, while a 5 min growth process resulted in 40–50 nm NGQDs. Nonetheless, since lignin and chitosan are long-chain biopolymers, the synthesis approach can be considered a combination of the top–down and bottom–up approaches.

Although natural resources can serve as sustainable feedstock for the production of GQDs, the available synthesis methods still require high temperatures and long reaction times. Microplasma, which is defined as a gaseous discharge with one of its dimensions spatially confined to a scale of less than a millimeter [56], has emerged as a suitable candidate for the synthesis of GQDs [31,57]. The special feature of a non-equilibrium regime (gas temperature < electron temperature) enables the generation of highly reactive species (e.g., electrons, ions and radicals) in great density even at low levels of energy consumption and under ambient conditions [58–61], which is suitable for sustainable colloidal nanomaterial syntheses, such as carbon-, silicon- and metal-based nanoparticles [57,62–65]. Figure 4d demonstrates findings from our recent publication about the synthesis of NGQDs from chitosan using microplasma under ambient conditions [66]. We proposed that the plasma-generated reactive species were responsible for initiating the bond scission of the glycosidic linkage of chitosan and the formation of NGQDs from chitosan fragments. Furthermore, by adjusting the pH value of the electrolyte solution, a different plasma-liquid chemistry could occur, producing tunable emissions from 441 to 561 nm and controllable functionalities of NGQDs [57,67]. This microplasma technology is also applicable to other precursors, such as bioresources (starch, citric acid, lignin, fructose and cellulose) [68,69] and organosulfate [70,71], and has the potential for industrial-scale applications via microplasma arrays complemented with microfluidic devices [72–74]. For the reader's convenience, all the aforementioned synthesis methods of GQDs are further summarized in Table 1.

**Table 1.** Summary of different synthesis methods of GQDs from various precursors and the corresponding resulting GQDs' properties.

| No. | Precursors | Synthesis Methods | Reaction Conditions | Materials | Yield (%) | GQDs Properties | | | Ref. |
|---|---|---|---|---|---|---|---|---|---|
| | | | | | | Size (nm) | Emission (nm) | PLQY (%) | |
| 1 | Coal | Chemical exfoliation | 24 h 100–120 °C | GQDs | 10–20 | 2.3–2.9 | 460–500 | 1.0 | [42] |
| 2 | Coke | Electrochemical exfoliation | 1 h 40 mA cm$^{-2}$ | o-GQDs | 31.1 | 4.6 | 560 | 9.2 | [44] |
| | | | 1 h 120 mA cm$^{-2}$ | y-GQDs | 42.9 | 4.2 | 530 | 7.9 | |
| | | | 1 h 240 mA cm$^{-2}$ | g-GQDs | 17.9 | 3.0 | 500 | 8.5 | |
| | | Reduction of G-GQDs with NaBH$_4$ | 4 h | b-GQDs | 13.0 | 2.9 | 440 | 19.3 | |
| 3 | Graphene | Hydrothermal | 10 h 200 °C | GQDs | 22 | 9.6 | 430 | 6.9 | [6] |
| 4 | MWCNT | Two-steps electrochemical | 17 h 1 V; 90 °C | GQDs | 30–38 | 3.0 | 455 | 6.3 | [46] |
| | | | 13 h 1 V; 90 °C | GQDs | | 5.2 | 425 | 5.9 | |
| | | | 9 h 1 V; 90 °C | GQDs | | 8.2 | 400 | 5.4 | |
| | | | 17 h 1 V; 30 °C | GQDs | | 23.0 | 385 | 5.1 | |
| 5 | CF | Chemical exfoliation | 24 h 120 °C | GQDs | n.a. | 3.0 | 434 | n.a. | [48] |
| | | | 24 h 100 °C | GQDs | n.a. | 6.0 | 500 | n.a. | |
| | | | 24 h 80 °C | GQDs | n.a. | 9.0 | 564 | n.a. | |
| 6 | Trinitropyrene in NaOH | Hydrothermal | 10 h 200 °C | b-GQDs | 45 | 2.6 | 450 | 21 | [49] |
| | Trinitropyrene in hydrazine and ammonia | | | c-GQDs | 56 | 2.9 | 475 | 45 | |
| | Trinitropyrene in NaOH | | 1 h 200 °C | g-GQDs | 63 | 3.5 | n.a. | 23 | |
| | Trinitropyrene in ammonia | | 10 h 200 °C | y-GQDs | 60 | 3.8 | 535 | 7 | |

**Table 1.** *Cont.*

| No. | Precursors | Synthesis Methods | Reaction Conditions | Materials | Yield (%) | GQDs Properties | | | Ref. |
|---|---|---|---|---|---|---|---|---|---|
| | | | | | | Size (nm) | Emission (nm) | PLQY (%) | |
| 7 | Trinitropyrene, thiourea, DMF, NaOH | Hydrothermal | 10 h 200 °C | N, S-GQDs | 87.8 | 2.1 | 450 | 23.2 | [50] |
| 8 | Citric acid | Pyrolysis | 30 min 200 °C | GQDs | n.a. | 15 | 460 | 9 | [52] |
| 9 | Glucose | Microwave-assisted hydrothermal | 5 min 595 W | GQDs | n.a. | 3.4 | 473 | 11 | [53] |
| 10 | Lignin | Oxidized cleavage + hydrothermal | 12 + 12 h 180 °C | NGQDs | 21 | 3.7 | 410 | 21 | [54] |
| | | | 12 + 1 h 180 °C | | n.a. | 4.4 | 430 | n.a. | |
| 11 | Chitosan | CVD | 3 min 250–300 °C | NGQDs | n.a. | 10–15 | 448 | n.a. | [55] |
| 12 | Chitosan | Microplasma | 1 h 9.6 mA | NGQDs | 50 | 6.4 | 532 | 30 | [57] |
| 13 | Fructose | Microplasma | 1 h 9.6 mA | GQDs | 16.6 | 4.5 | 446 | 0.9 | [69] |
| | Citric acid | | | NGQDs | 28.1 | 3.6 | 516 | 2.6 | |
| | Lignin | | 1 h 5 mA | N, S-GQDs | 58.7 | 3.1 | 514 | 1.0 | |
| | Cellulose | | 1 h 10 mA | GQDs | 3.0 | n.a. | 428 | 1.2 | |
| | Starch | | 1 h 9.6 mA | GQDs | 50.9 | 4.1 | 558 | 27.5 | |

o-GQDs stands for orange-emission GQDs; y-GQDs stands for yellow-emission GQDs; g-GQDs stands for green-emission GQDs; b-GQDs stands for blue-emission GQDs; c-GQDs stands for cyan-emission GQDs; N, S-GQDs stands for N, S co-doped GQDs; n.a. stands for not available.
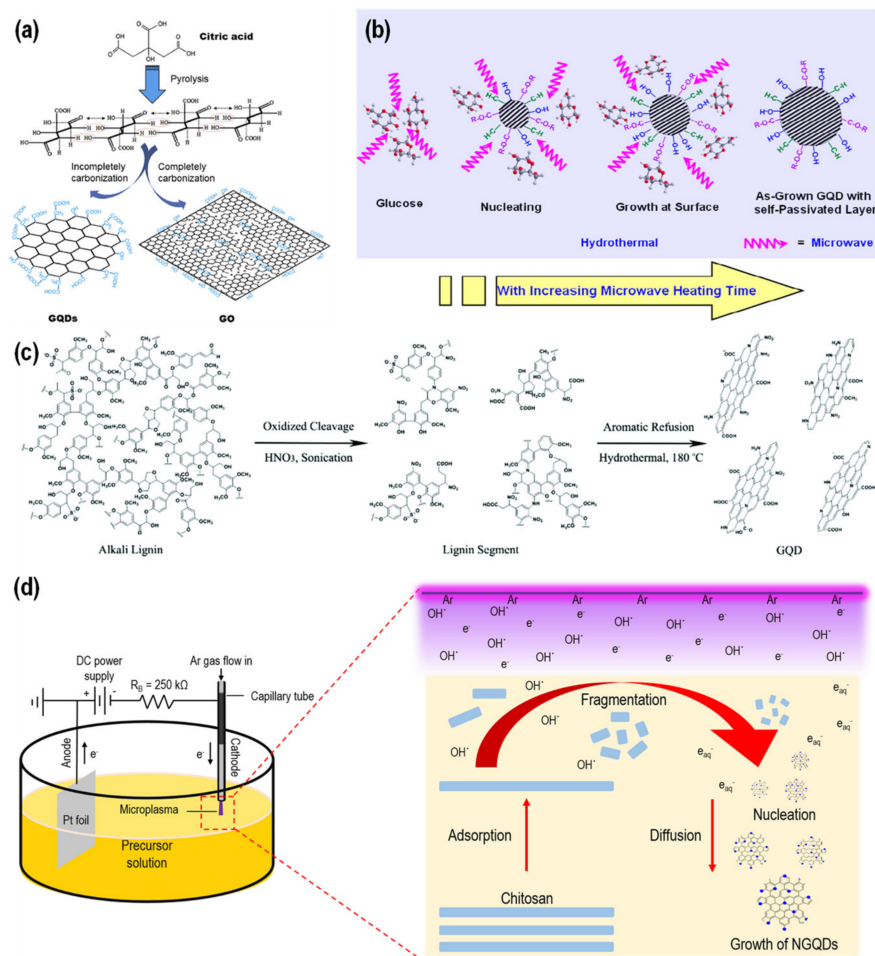
**Figure 4.** Synthesis of GQDs based on bottom–up approach using natural resources. GQDs synthesis from (**a**) citric acid [52], (**b**) glucose [53], (**c**) lignin [54], and (**d**) chitosan [66].

Based on the above discussion and the summary provided in Table 1, it can be inferred that the bottom–up approach offers several advantages compared to the top–down approach, including broad precursors, especially from naturally available bioresources, a relatively higher production yield and higher functionalization possibilities. Although it is possible to produce GQDs in the yellow emission range through the bottom–up approach, it is challenging to produce orange- or even red-emission GQDs. Most of the GQDs synthesized via the bottom–up approach exhibit blue or green emissions; the opposite is true for the top–down approach. On the other hand, the hydrothermal method is probably the most commonly used for the synthesis of GQDs via a bottom–up approach, yet the necessities of a high temperature and long reaction time are major setbacks to its practicality in relation to large-scale production. Therefore, the microwave technique can be employed together with the hydrothermal method to speed up the reaction rate, yet its availability is still a challenge for large-scale production. Microplasma emerges as a promising candidate for the synthesis of GQDs due to its rapidity, environmental friendliness, sustainability, controllability and ease of functionalization. Coupled with the implementation of a microplasma array and microfluidic technology, microplasma has great potential for large-scale production. However, microplasma might be precursor-dependent, in which one precursor might result in a high production yield of GQDs, while another precursor might result in a low production yield. Therefore, no synthesis method can be considered to be the best. Each synthesis method has advantages and disadvantages that may be suitable for a particular purpose but not others.

## 4. Fabrication of GQD Nanocomposites

Whilst GQDs are already useful for many applications, their performance, practicality and versatility can be further improved by integrating them with organic or inorganic materials to produce GQD nanocomposites. Moreover, a broader application scope can also be expected. The combination of GQDs with polymeric matrices is the most commonly used method to fabricate GQD nanocomposites with organic molecules. The primary objective for the utilization of polymeric matrices is to provide 3D templates, in which the embedded GQDs can act as sensor probes upon external stimulation, resulting in a broadened application scope and enhanced practicality. Many studies have also reported that GQD nanocomposites can yield better mechanical properties than the corresponding pristine polymers because GQDs can act as nanocross-linkers due to the presence of surface-functional groups. As a result, various chemical and physical interactions can occur between the functional groups of GQDs and side chains of polymers. On the other hand, GQDs can also be integrated with inorganic molecules, such as metal nanoparticles, to enrich their physico-chemical properties. Their exclusive characteristics and properties can complement and interact with each other, yielding a synergetic effect for better application performances. The fabrication of these GQD nanocomposites will be discussed in the following section.

### 4.1. GQD Nanocomposites with Organic Materials

The utilization of polymeric matrices to host GQDs is essential for supporting functions, improving the practicality of the applications. Films and gels are probably the most common forms of GQD nanocomposites and they have been developed and proved to be useful for broad applications. Although there are several methods for the fabrication of GQD-polymer composites [75], such as physical blending, chemical grafting and polymerization, physical blending can be considered the easiest and simplest process among them. Unlike the chemical grafting and polymerization methods, where a basic or even deep understanding of polymer chemistry is demanded, physical blending enables people from different disciplines without any basic polymer chemistry knowledge to successfully conduct the process.

Owing to its high water solubility and optical transparency, poly(vinyl alcohol) (PVA) has been widely used as the polymeric matrix to host GQDs [76–78]. Chen et al. fabricated thin luminescent films with a thickness of approximately 1.2 mm based on GQDs blended with PVA [77]. As shown in Figure 5a, the fabricated nanocomposite film was bendable, suggesting an excellent flexibility of the GQD/PVA nanocomposite. PVA also possesses a high optical transparency of up to 90% transmittance in the whole visible range (Figure 5b) [76]. However, as the content of GQDs in the nanocomposite film increases, the optical transparency gradually decreases (Figure 5b) [76]. Therefore, when one desires to fabricate a luminescent-GQD film with high optical transparency, the content of GQDs should be considered. Another study conducted by Nair et al. revealed that the initial cyan emission of the fabricated SGQD/PVA nanocomposite film could be altered to a green emission by increasing the content of SGQDs [78], as depicted in Figure 5c. This phenomenon is probably due to the particle agglomeration at a higher loading content [76], causing a red-shifting behavior of the PL property [79].

Meanwhile, the capability of the matrix to mimic human skin, which is able to be stretched and self-heal at room temperature, is demanded in the development of modern sensor technology. In this regard, Laysandra et al. designed a block co-polymer based on poly($n$-butyl acrylate)-$co$-poly[$N$-(hydroxymethyl)acrylamide] (PBA$_x$-$co$-PNMA$_y$) which was able to realize the aforementioned properties [80]. By collaborating with our group, the designed PBA$_{0.8}$-$co$-PNMA$_{0.2}$ (PBA:PNMA = 0.8:0.2) was further utilized to host plasma-assisted chitosan-derived NGQDs via a simple blending method, yielding a bright blue luminescent nanocomposite film with stretchable and self-healable properties (Figure 6a) [81], mimicking the human skin. Figure 6b also shows the good optical transparency of the developed nanocomposite films. Moreover, the surface-functional groups

on the NGQDs could form various chemical and physical bonds with the side chains of PBA$_{0.8}$-*co*-PNMA$_{0.2}$ during cross-linking, strengthening the mechanical performance with increasing the loading content of NGQDs (Figure 6c). As demonstrated in Figure 6d, the nanocomposite film was also able to completely self-heal for 24 h at room temperature after being cut, showing great potential as a wearable artificial skin sensor.
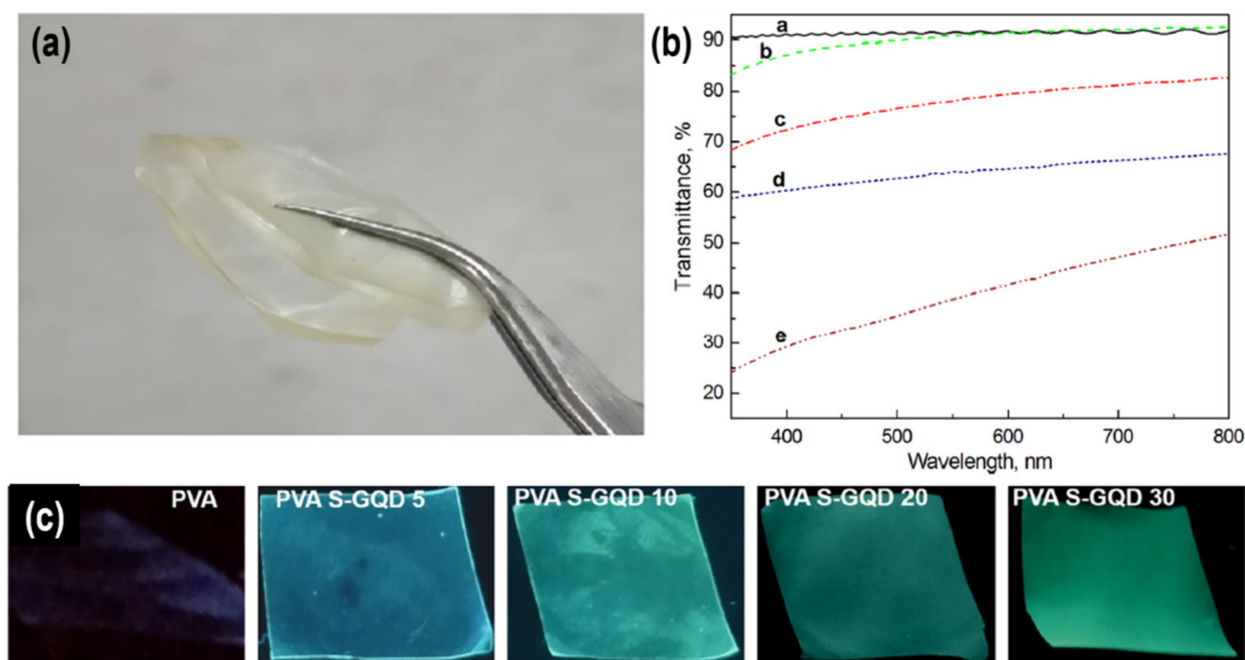


**Figure 5.** Fabrication of GQD/PVA nanocomposite films. (**a**) Excellent flexibility of the nanocomposite film [77]. (**b**) Optical transparency of (a) PVA film and GQD/PVA nanocomposite film with (b) 3, (c) 5, (d) 15 and (e) 25 wt% GQDs concentration [76]. (**c**) Visual images of nanocomposite films with different SGQDs content [78].

*4.2. GQD Nanocomposites with Inorganic Materials*

The fabrication of GQD nanocomposites with inorganic molecules can generally be classified into in situ and ex situ preparations. The former involves mixing the pre-synthesized GQDs with the precursor of inorganic nanomaterials to produce nanocomposites or vice versa. For example, Ge et al. firstly synthesized GQDs via the electrochemical cutting of graphene film [82]; then, an AgNO$_3$ aqueous solution was added into the GQD solution and stirred for 1 h to obtain Ag$^+$-GQDs (Figure 7a) [83]. Afterwards, the mixture was subjected to a photochemical reaction using 365 nm of 18 W UV irradiation at a distance of 20 mm for 3 h to form Ag-GQDs nanocomposites that could be used for a SERS application, which will be further discussed in a later section. Based on the TEM results in Figure 7b, it was revealed that the morphology of the nanocomposites consisted of an isolated larger particle approximately 10–30 nm being surrounded by smaller particles of 1–4 nm. The authors attributed the larger and smaller particles to AgNP and GQDs due to the lattice fringe of 0.24 and 0.33 nm corresponding to the (111) and (002) planes of Ag and graphite, respectively (Figure 7c). A similar morphology was reported by Jin et al. [84], where nanocomposites were formed from the hydrothermal treatment of a mixture of pre-made GQDs and AgNO$_3$ at 120 °C for 30 min. The authors further elaborated that their nanocomposites were core-shell nanostructured (~10 nm) with the AgNP as the core and GQDs as the shell.
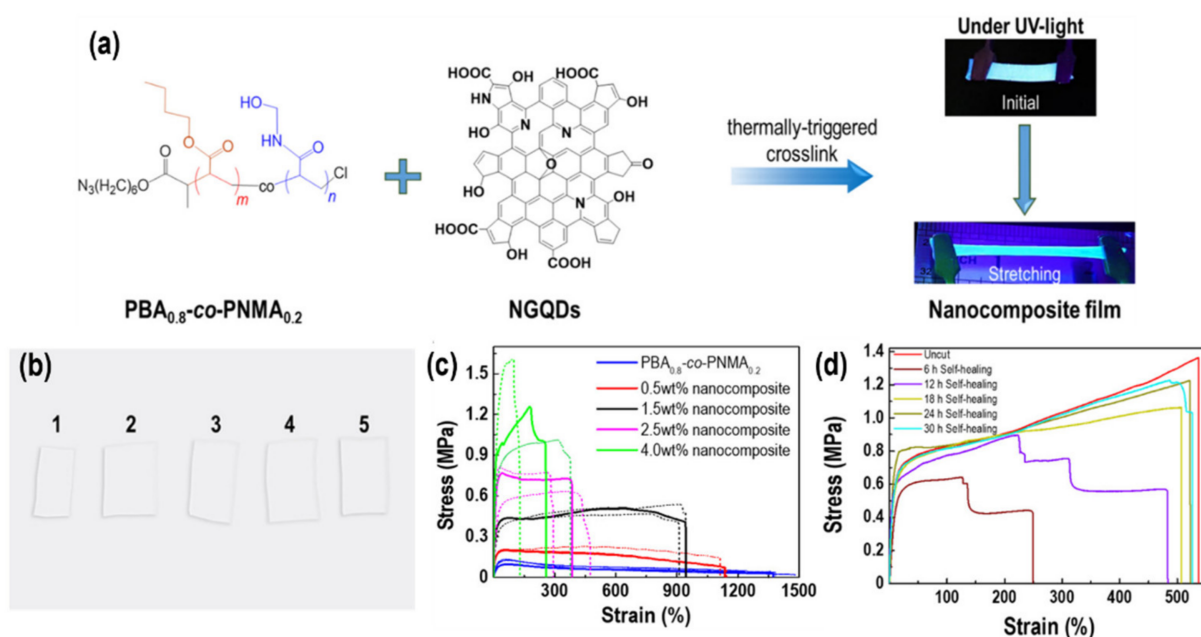
**Figure 6.** Fabrication of skin-like GQD-based nanocomposite film [81]. (**a**) Preparation of the stretchable NGQDs/PBA$_{0.8}$-*co*-PNMA$_{0.2}$ nanocomposite film. (**b**) Optical transparency of (1) PBA$_{0.8}$-*co*-PNMA$_{0.2}$ film and NGQDs/PBA$_{0.8}$-*co*-PNMA$_{0.2}$ nanocomposite films with (2) 0.5, (3) 1.5, (4) 2.5 and (5) 4.0 wt% NGQDs content. Stress–strain curve of the nanocomposite with (**c**) different NGQDs content and (**d**) with 1.5 wt% NGQDs content using different healing times at room temperature. The solid lines in subfigure (**c**) represent the best mechanical performance among three times measurement, whereas the dotted lines represent the other two mechanical performances to suggest the reproducibility and stability.

In the study conducted by Miao et al. [85], AuNPs with an average size of 40 nm were prepared first from HAuCl$_4$ through a hydrothermal method, followed by mixing with cetyltrimethylammonium bromide (CTAB) and heating in an oven at 165 °C for 1 h to grow NGQDs on the surface of AuNPs, as illustrated in Figure 7d. The added CTAB protected the AuNPs during the hydrothermal treatment and simultaneously functioned as the carbon and nitrogen source for the formation of NGQDs. The TEM, STEM-HAADF and STEM-EDX images in Figure 7e prove that the NGQDs had successfully grown on the Au surface. A similar result was also reported by Das et al., despite the difference of synthesizing the NGQDs first, which was followed by the addition of HAuCl$_4$ into the NGQD solution to fabricate Au@NGQD nanocomposites using a hydrothermal method at 110 °C [86].
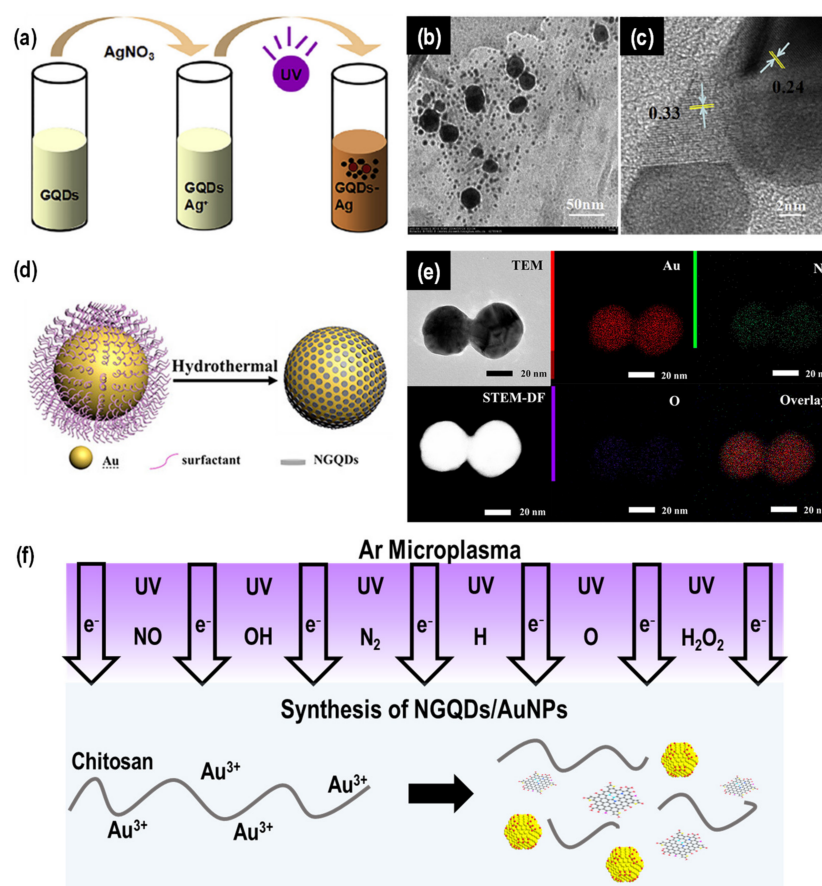
**Figure 7.** In situ preparation of GQD-inorganic nanocomposites. (**a**) Schematic illustration of the synthesis of Ag-GQD nanocomposites [83]. (**b**) TEM and (**c**) HRTEM images of Ag-GQDs [83]. (**d**) Schematic illustration of the synthesis of Au-NGQD nanocomposites [85]. (**e**) TEM, STEM-HAADF, Au, N, O and overlay elemental mapping of Au-NGQDs [85]. (**f**) Schematic illustration of microplasma-based technologies for the fabrication of NGQD/AuNP nanocomposites [87].

As mentioned in the previous section, microplasma is a versatile technology for the synthesis of colloidal GQDs. Nonetheless, this technology can also be extended to the fabrication of GQD nanocomposites. Our group utilized this microplasma technology to fabricate an Au@GQD nanocomposite in an environmentally friendly manner at ambient conditions [88]. In the typical procedure, the GQDs were firstly synthesized by treating starch electrolyte with a microplasma electrochemical reactor for 60 min. After the post-treatment process, the purified GQDs were mixed with $HAuCl_4$ and the obtained mixture was further treated with microplasma for 3 min to produce Au@GQD nanocomposites. In addition, our group recently reported about microplasma-derived bioresource AuNP/NGQD nanocomposites with multifunctional properties [87]. Chitosan, as the main carbon and nitrogen source for the synthesis of NGQDs, was mixed with $HAuCl_4$. The mixture was then subjected to a microplasma treatment for 20 min to produce NGQDs/AuNPs (Figure 7f). By neutralizing the plasma-treated solution, the unreacted chitosan could be converted into hydrogel and the NGQDs/AuNPs were simultaneously embedded into the hydrogel. Owing to the synergetic effect of the plasma-generated reactive species and various interactions between the functional groups of NGQDs/AuNPs with the side chains of chitosan, further cross-linking the composite hydrogel with microplasma could lead to a significant mechanical enhancement of the nanocomposites. Finally, NGQD/AuNP sponges could be obtained by freeze-thawing the NGQD/AuNP hydrogel.

Meanwhile, the ex situ preparation refers to the formation of nanocomposites by mixing both the pre-synthesized GQDs and inorganic nanomaterials. These two distinct

nanomaterials can be bonded either physically via non-covalent interactions (e.g., hydrogen bonds and electrostatic forces) or chemically via covalent interactions. Wang et al. separately synthesized AgNPs and GQDs, and further aminated the surface of the AgNPs with 3-aminopropyltriethoxysilane (APTES) to yield Ag-NH$_2$ NPs [89]. To finally obtain Ag@GQDs core-shell nanocomposites, the Ag-NH$_2$ NPs and GQDs were mixed and stirred at room temperature for 24 h. The procedure is schematically shown in Figure 8a. A similar strategy was employed by Liu et al. to produce AuNPs/glycine derivative/GQDs (AuNPs/G$_n$/GQDs) nanocomposites (Figure 8b) [90]. In this case, glycine, as an amino acid, was utilized as a bridge to connect the AuNPs and GQDs. Therefore, the distance between the AuNPs and the GQDs could be effectively adjusted by simply changing the chain length of G$_n$, resulting in controllable PL and SERS responses. The typical procedure involves the addition of G$_n$ into the pre-synthesized AuNPs with 30 min of incubation followed by the addition of the pre-synthesized GQDs and incubation for 5 min at room temperature.
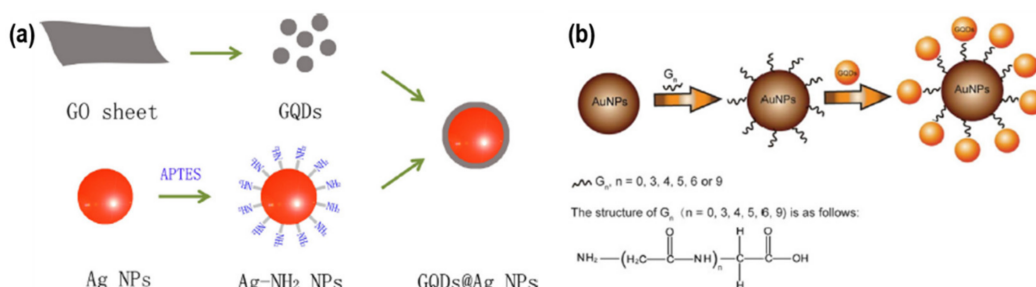


**Figure 8.** Ex situ preparation of GQD-inorganic nanocomposites. Schematic illustration of the synthesis of (**a**) Ag@GQDs core shell [89] and (**b**) AuNP/G$_n$/GQDs nanocomposites [90].

## 5. Luminescence-Based Biosensing Applications of GQD Nanocomposites

In addition to being cost-effective, GQD nanocomposites as biosensors also allow the real-time analysis and sensitive detection of target biomarkers for medical and diagnostic applications. By simplifying the detection method, the key properties of the biosensor, such as selectivity, sensitivity and reproducibility, are enhanced [8]. In this section, we will cover various luminescence-based techniques for biosensing applications of GQD nanocomposites, including PL, CL and ECL.

### 5.1. Photoluminescence (PL)

PL describes a radiative recombination process of a molecule upon photon excitation. Dopamine is an important neurotransmitter biomarker which regulates the function of the central nervous system. Real monitoring of this molecule within the physiological concentration is essential to avoid several diseases such as schizophrenia and Parkinson's disease. Das et al. synthesized Au@NGQDs core-shell nanocomposites for the sensitive detection of dopamine from 1.0 to 100.0 with a limit of detection (LoD) of 430 nM. Moreover, the developed nanocomposites were also usable for DA detection in human serum over a concentration range of 10–80 µM with an LoD of 590 nM, which is approximately 27-times lower than the lowest abnormal concentration of DA in serum (16 µM) [86]. Sun et al. used a combination of GQDs and a Au nanoflower (AuNF) for the detection of miRNA-34a by exploiting a fluorescence resonance energy transfer (FRET) [91]. In their detection system, the probe was firstly prepared by conjugating a AuNF with several GQDs via a DNA hybridization method of two single-strand DNAs (ssDNA1 and ssDNA2) with a DNA linker-strand. Through this hybridization, the GQDs could be brought close to the AuNF with a distance of approximately 4 nm, promoting PL quenching (the "off" state) of GQDs due to the energy transfer from the excited dipole of GQDs to the AuNF. However, after the introduction of miRNA-34a, multiple GQDs were detached from the AuNF via toehold-mediated DNA strand displacement, causing a significant PL enhancement of GQDs (the "on state") due to the absence of a FRET mechanism, which was linearly proportional

to the increment of the miRNA-34a concentration from 0.4 to 4 fM with an LoD of 0.1 fM (Figure 9a,b). This developed detection platform enabled the reliable early diagnosis of cardiovascular diseases.
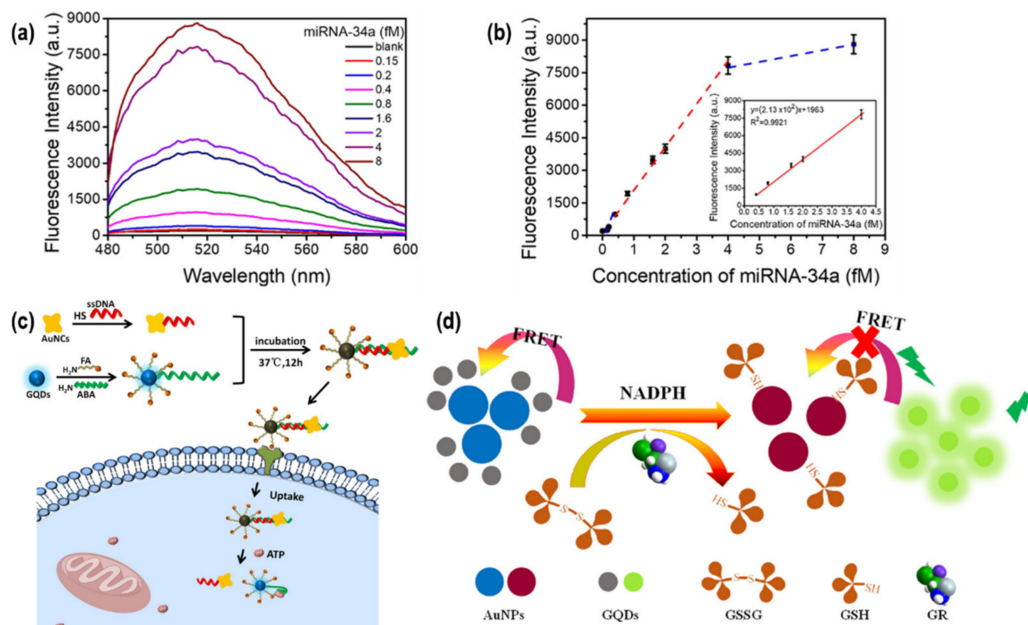


**Figure 9.** GQD nanocomposites as PL-based biosensors. (**a**) PL spectra and (**b**) the corresponding PL intensity of AuNF@GQDs in the presence of different concentrations of miRNA-34a [91]. The dashed lines in subfigure (**b**) represent the fluorescence intensity dependency on the miRNA-34a concentrations from 0 to 8 fM, while the solid line represents the linear detection range from 0.4 to 4 fM (inset). Schematic illustration of (**c**) the AuNCs-GQDs nanocomposites for intracellular-ATP sensing [92], and (**d**) GQDs-AuNPs nanocomposites for GR detection [93].

A similar "off–on" technique was reported by Zhang et al. for the detection of intracellular adenosine triphosphate (ATP) using GQDs and Au nanocrosses (AuNCs), as shown in Figure 9c [92]. The initially low PL emission of AuNCs-GQDs was gradually enhanced as the concentration of ATP increased. As a result, a linear detection of ATP from 0.3 to 2.0 mM with an LoD of 0.27 mM could be established. The authors further proved that their developed nanocomposites were biocompatible and still demonstrated high selectivity towards ATP even in the presence of interferences. Since ATP provides energy and participates in the metabolism of fats, protein, sugar and nucleic acid in the cells, ATP can serve as an important biomarker in apoptosis, necrosis and cancer diagnostics.

Yan et al. combined GQDs with AuNPs to probe glutathione reductase (GR) activity [93]. A similar FRET mechanism as discussed above was exploited as the underlining sensing mechanism (Figure 9d). The addition of GQDs into a AuNPs solution could induce the aggregation of GQDs and AuNPs, resulting in PL quenching through a FRET mechanism. However, in this work, an additional catalytic reduction of oxidized glutathione (GSSH) into reduced glutathione (GSH) with GR was employed in the presence of coenzyme β-nicotinamide adenine dinucleotide 2′-phospate hydrate (NADPH). The yielded GSH could enlarge the inter-particle distance between AuNPs and GQDs, resulting in the PL recovery of GQDs. The proposed sensing strategy could be used for probing GR activity in the range of 0.005–0.13 mU/mL with an LoD of 0.005 mU/mL, showing great potential not only for monitoring the genesis of anxiety and biological oxidative stress, but also malignant tumor cells.

On the other hand, another work conducted by Abdolmohammad-Zadeh et al. integrated GQDs with a zirconium-based metal-organic framework (GQDs/UiO-66) to enable photocatalytic activity in a peroxidase mimetic-based PL analysis of $H_2O_2$ [94]. Due to

the fact that $H_2O_2$ is a product of the enzymatic oxidation of cholesterol, the plausibility of detecting $H_2O_2$ can eventually lead to the indirect detection of cholesterol through catalyzing the oxidation of terephthalic acid (TA). The oxidation of TA can lead to the production of a highly fluorescent product; thus, the PL intensity will be indirectly proportional to the concentration of $H_2O_2$, and, subsequently, the concentration of cholesterol in the presence of cholesterol oxidase within 0.04–1.60 µmol/L with an LoD of 0.01 µmol/L. This kind of peroxidase mimetic technique is also applicable for the indirect detection of glucose in the presence of glucose peroxidase [95–97]. Another recent study conducted by Adel et al. reported direct PL-based cholesterol sensing using NGQDs and copper indium sulfide/zinc sulfide (CIS/ZnS) QDs nanocomposites (NG/CIS/ZnS QD) [98]. In this study, the PL intensity of NG/CIS/ZnS QD nanocomposites was quenched after incubating them with cholesterol molecules, showing a linear correlation from 0.312 to 5 mM with an LoD of 0.222 mM. The sensing mechanism was attributed to the chemical reaction between the hydroxyl groups and carboxylic or amine groups of cholesterol and nanocomposite QDs, respectively, promoting the agglomeration of QDs that, subsequently, led to the destabilization of the surface charge and PL quenching of the nanocomposite QDs. Table 2 summarizes the recent works about GQD nanocomposites as PL-based biosensors.

**Table 2.** Summary of the GQD nanocomposites for PL-based biosensing applications.

| Biosensors | Analyte | Linear Range | LoD | Ref. |
|---|---|---|---|---|
| Au@NGQDs | DA | 1.0–100.0 µM | 430 nM | [86] |
| AuNF@GQDs | miRNA-34a | 0.4–4 fM | 0.1 fM | [91] |
| AuNCs-GQDs | ATP | 0.3–2.0 mM | 0.27 mM | [92] |
| GQDs-AuNPs | GR | 0.005–0.13 mU/mL | 0.005 mU/mL | [93] |
| GQDs/UiO-66 | Cholesterol | 0.04–1.60 µmol/L | 0.01 µmol/L | [94] |
| NG/CIS/ZnS QD | Cholesterol | 0.312–5 mM | 0.222 mM | [98] |
| Amine NGQDs@AuNPs | Neuron-specific enolase (NSE) | 0.1–1000 ng/mL | 0.09 pg/mL | [99] |
| PEHA-GQD-His | miRNA-141 | $10^{-18}$–$10^{-12}$ M | $4.3 \times 10^{-19}$ M | [100] |
| NGQDs/CrPic | Cholesterol | 0–520 µM | 0.4 µM | [101] |

PEHA stands for pentaethylenehexamine; His stands for histidine; CrPic stands for chromium picolinate.

In collaboration with Chiu's group, we recently reported the fabrication of stretchable and self-healable NGQD nanocomposite films as wearable pH sensors (Figure 6) [81]. Although pH values do not belong to any biomolecules, they can still be used as indicators for wound infections on the skin and abnormalities in human sweat pH, which can suggest issues related to hydration status, skin diseases, kidney function and, especially, cystic fibrosis [102,103]. The NGQD nanocomposites demonstrated a 15-fold increase in pH detection sensitivity from pH 3 to 10 compared with pristine NGQDs. This remarkable sensing performance coupled with a high elasticity, enhanced mechanical strength and self-healable property at room temperature herald our nanocomposites with an innovative potential as artificial skin for wearable biosensors.

### 5.2. Chemiluminescence (CL)

CL is a phenomenon of light radiation following a chemical reaction. The process involves the electron excitation of a molecule from the ground state to the excited state due to the absorption of energy resulting from a chemical reaction. One significant advantage of CL is the zero background light scattering interference caused by the absence of an excitation light source [104–106]. Nevertheless, one notable drawback of CL is its need for additional chemical reagents, influencing some chemical and physical parameters that may cause fluctuations during sensing. In the chemical parameter aspect, the added CL reagent is not exclusive to one unique analyte (low selectivity) and the corresponding CL intensities are sensitive to pH, temperature, ionic strength, solvent and other components contained in the system [104]. Meanwhile, with regard to physical parameters, the chemical reaction time may affect CL intensity, with the intensity potentially increasing at the beginning, reaching

the maximum threshold, then decreasing afterwards [104]. In addition, the added chemical reagents may also possess some cytotoxicity, which limits the utilization of CL for in vivo detection [107]. As a consequence, only a few works on CL-based GQD nanocomposite biosensors have been reported.

Sun et al. successfully fabricated hemin/G-quadruplex DNAzyme modified sandwich-rod GQDs@GO@CF nanocomposites (DNAzyme/L-Apt/GQDs@GO@CF) for the detection of lysozyme (LZM) (Figure 10a) [108]. LZM, which is an alkaline enzyme in pathogenic bacteria, is a marker for various kinds of acute leukemia, renal tubular damage, high lysozyme hyperlipidemia and other diseases. The GQDs@GO@CF functioned as a supporting material to provide a large binding site for L-Apt, which acted as a specific recognition element to improve the selectivity, while the DNAzyme was a signal amplifier and catalyst for the CL reaction of luminal-$H_2O_2$. As depicted in Figure 10b, DNAzyme was formed when hemin was bounded to G-quadruplex DNA. The coordination of guanine to heme iron contributed to the high peroxidase activity. Then, in the presence of $H_2O_2$, intermediate DNAzyme-$H_2O_2$ was generated and oxidized the luminol into a luminol-acid radical under alkaline conditions, generating a strong CL signal. Under the optimized conditions, a linear detection of lysozyme in the range of 0.26–66 ng/L with an LoD of 12.5 pg/L could be obtained.
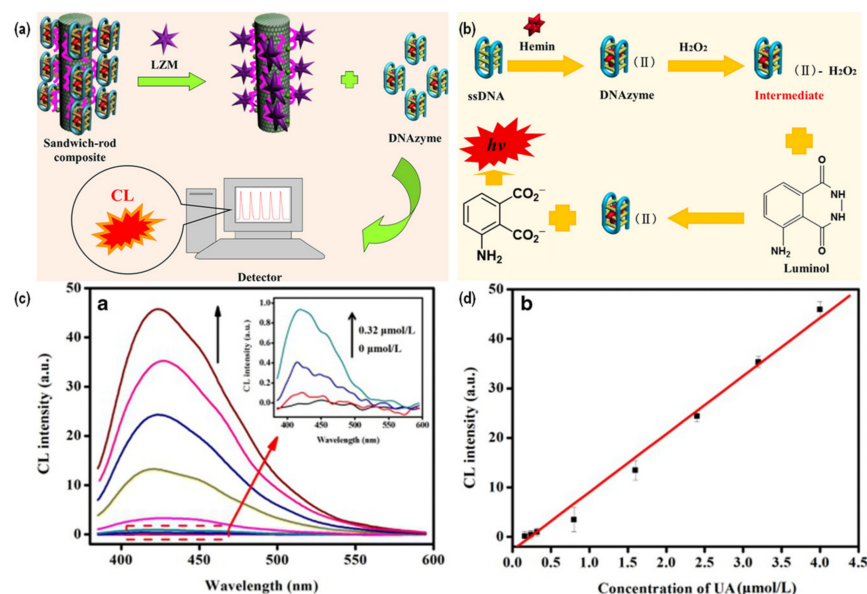


**Figure 10.** GQD nanocomposites as CL-based biosensors. Schematic illustration of (**a**) DNAzyme/L-Apt/GQDs@GO@CF for CL-based detection of LZM and (**b**) the corresponding CL mechanism [108]. (**c**) CL spectra of Cu(II)/Cu$_2$O/NGQDs nanocomposites in the presence of different concentrations of UA, including 0 (black), 0.16 (red), 0.24 (blue), 0.32 (dark cyan), 0.8 (magenta), 1.6 (dark yellow), 2.4 (navy), 3.2 (pink), and 4.0 μM (wine), and (**d**) the corresponding linear plot of the CL intensity at 422 nm with respect to UA concentration [109].

Shi et al. designed a uric acid (UA) biosensor based on the oxidation of UA in the presence of uricase to form $H_2O_2$ [109]. They prepared Cu(II)/Cu$_2$O/NGQDs nanocomposites to mimic peroxidase activity in the luminol-$H_2O_2$ CL system. The presence of NGQDs in the nanocomposites enhanced their electronic conductivity, facilitating the catalysis reaction to generate reactive oxygen species. It was observed that the CL spectra were increasing with increasing concentrations of UA (Figure 10c), exhibiting a linear correlation from 0.16 to 4.0 μM with an LoD of 41 nM (Figure 10d). This developed biosensor was usable in real-time monitoring of UA in both human serum and urine. Table 3 summarizes the reported works about GQD nanocomposites as CL-based biosensors.

**Table 3.** Summary of the GQD nanocomposites for CL-based biosensing applications.

| Biosensors | Analyte | Linear Range | LoD | Ref. |
|---|---|---|---|---|
| DNAzyme/ L-Apt/GQDs@GO@CF | LZM | 0.26–66 ng/L | 12.5 pg/L | [108] |
| Cu(II)/$Cu_2O$/NGQDs | UA | 0.16–4.0 μM | 41 nM | [109] |
| GQDs/$MoS_2$ | Cholesterol | 0.08–300 μM | 35 nM | [110] |
| NC-$Fe_3O_4$@GQDs | Dopamine | 0.25–17.5 μg/L | 0.054 μg/L | [111] |

L-Apt stands for lysozyme aptamers; $MoS_2$ stands for molybdenum disulfide; NC stands for nanocellulose.

*5.3. Electrochemiluminescence (ECL)*

ECL, which is also called electrogenerated CL, involves the emission of reactive intermediates while undergoing electron transfer reactions at the electrode surface upon excitation by electrical energy [112]. This method is a combination of the advantages of electrochemistry and CL, providing fast response times, high sensitivity and selectivity, regeneration of ECL emitters, suppression of self-quenching from side reactions and no background light interferences [113]. As a nanomaterial for ECL biosensors, GQD is widely used as a luminescent material for ECL sensors because of its larger surface area, better biocompatibility and environmental friendliness compared to other quantum dots [114]. To improve luminescence efficiency, GQDs can also be linked with other bioactive substances or nanomaterials to form nanocomposite materials, which can greatly stabilize the ECL emissions. Among them, metal nanoparticles are widely used in sensor construction, as they can significantly increase the load of GQDs and enhance the signal amplification capability [115]. Therefore, these new nanocomposite materials offer lower cytotoxicity, better electron transfer capability and stronger luminescence signals compared with the conventional biosensors.

Zuo et al. developed a solid-state ECL biosensor for Concanavalin A (Con A) detection [116]. Con A is a member of the legume lectin family which has been widely used for clinical analysis of malignant tumor cells. In their study, GQDs were utilized as the luminophore, while AgNPs and $CeO_2$ nanospheres ($CeO_2$@AgNPs) were used as carriers to amplify the sensing signal by achieving the immobilization of GQDs, and glucose oxidase acted as a recognition element for capturing Con A (Figure 11a). Figure 11b shows that the ECL signal of the constructed GOx-$CeO_2$@Ag-GQDs nanocomposites increased with increasing concentrations of Con A, yielding a linear correlation in the range of 0.0005–1.0 ng/mL with an LoD of 0.16 pg/mL (Figure 11c).

On the other hand, Yang et al. successfully developed a novel ECL immunosensor based on a AuNP/GQDs-poly(etherimide)-GO (AuNP/GQDs-PEI-GO) nanocomposite to probe prostate-specific antigens (PSAs) [114]. PSAs are considered a significant biomarker for prostate cancer, where concentrations of PSA in normal healthy and prostate cancer suffering men are around <4.0 ng/mL and >10.0 ng/mL, respectively. To realize the detection of PSA, a poly(indole-6-carboxylic acid)/flower-like AuNPs (PICA/FGNs) composite was prepared and used as a suitable substrate for the immobilization of the primary antibody (Ab1) via an amide bond, while the AuNP/GQDs-PEI-GO nanocomposite was employed to immobilize the secondary antibody (Ab2). As a result, the specific sites of Ab1 and Ab2 could identify the PSA in the detection system, generating an ECL signal. Figure 12 schematically illustrates the ECL immunosensor design based on AuNP/GQDs-PEI-GO. Owing to the synergetic action of each component in the nanocomposite system, a broad PSA detection from 0.001 to 100 ng/mL with an LoD of 0.44 pg/mL could be achieved. Moreover, it was further demonstrated that the developed immunosensor could be used in actual human serum sample detection with good stability, reproducibility, selectivity and accuracy. Table 4 summarizes the reported works about GQD nanocomposites as ECL-based biosensors.
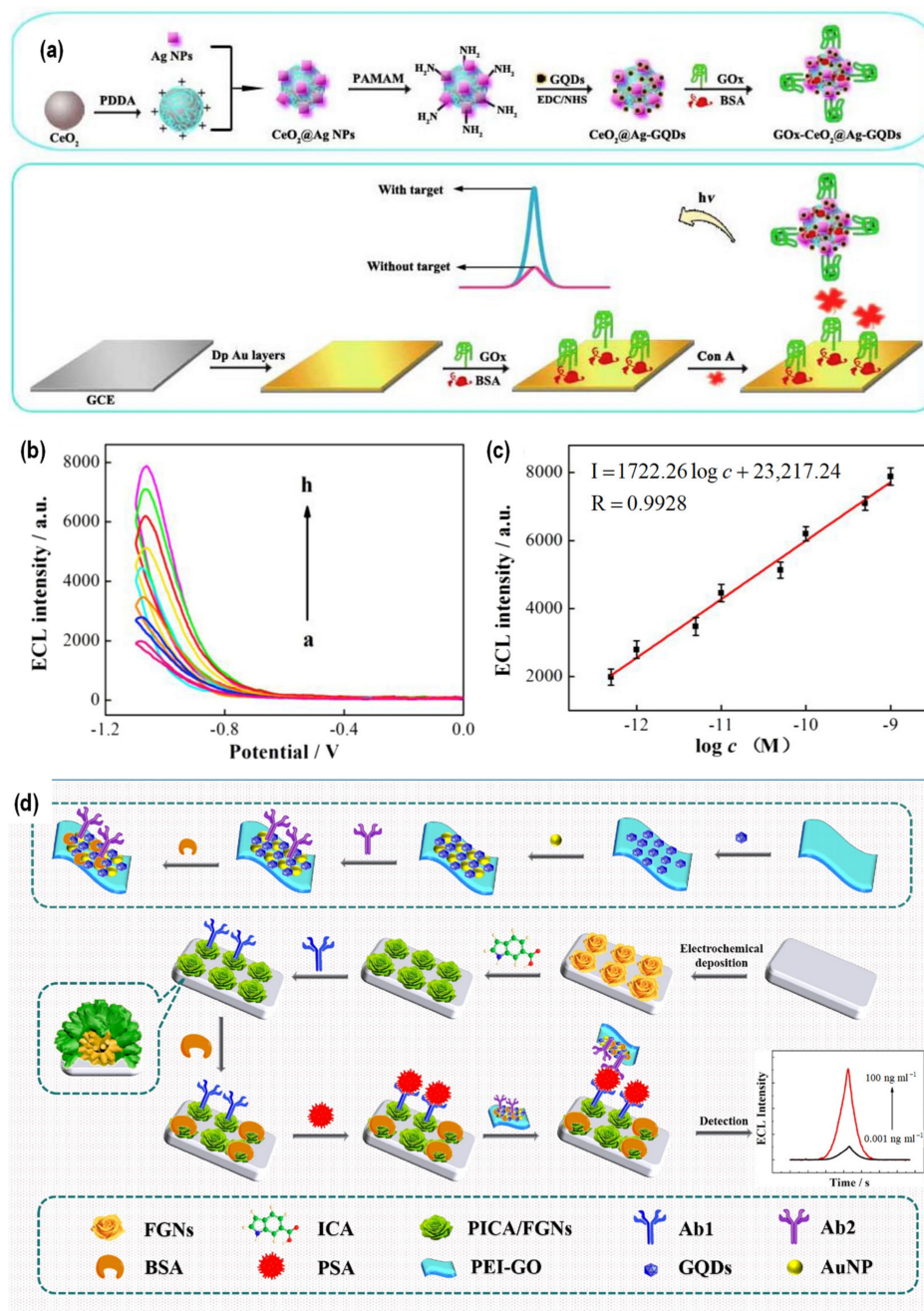
**Figure 11.** GQD nanocomposites as ECL-based biosensors. (**a**) Schematic illustration of the fabrication of GOx-CeO₂@Ag-GQDs nanocomposites for ECL-based detection of Con A. (**b**) ECL spectra of GOx-CeO₂@Ag-GQDs nanocomposites with different concentrations of Con A, including 0.5, 1.0, 5, 10, 50, 100, 500, 1000 pg/mL (from a to h). (**c**) The corresponding linear correlation between logarithmic Con A concentrations and ECL intensities of GOx-CeO₂@Ag-GQDs nanocomposites [116]. (**d**) Schematic illustration of the fabrication of ECL biosensor for PSA detection [114].
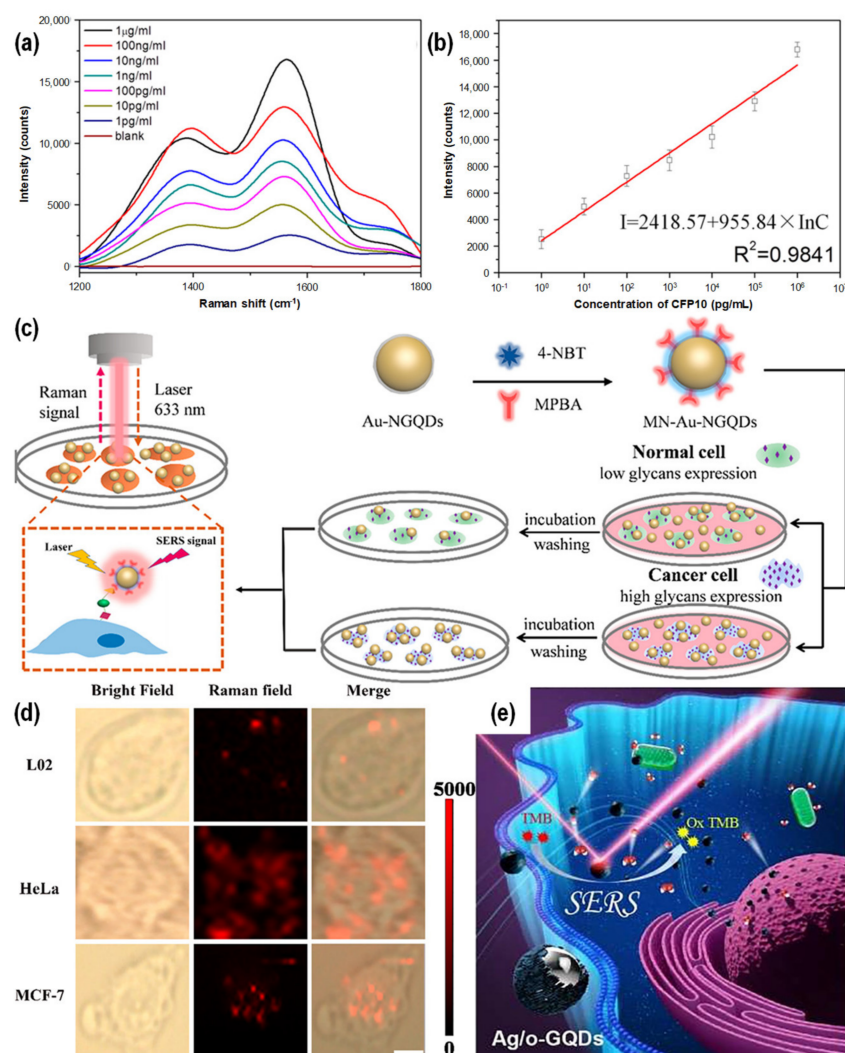
**Figure 12.** GQD nanocomposites as SERS-based biosensors. (**a**) SERS signal from different concentrations of CFP-10 antigen on $Fe_3O_4$-Au-GQDs nanocomposites and (**b**) the corresponding linear correlation between the logarithmic CFP-10 antigen concentrations versus Raman peak intensities at 1579 $cm^{-1}$ [117]. (**c**) Schematic illustration of SERS imaging on cellular surface glycans and (**d**) the corresponding SERS mapping images of single L02, HeLa, and MCF-7 cell based on the intensity of 1333 $cm^{-1}$ [85]. (**e**) Schematic illustration of the SERS activity of Ag/o-GQDs nanocomposites for in situ catalytic oxidation of TMB for monitoring $H_2O_2$ in cancer cell [84].

**Table 4.** Summary of the GQD nanocomposites for ECL-based biosensing applications.

| Biosensors | Analyte | Linear Range | LoD | Ref. |
|---|---|---|---|---|
| GOx-CeO$_2$@Ag-GQDs | Con A | 0.0005–1.0 ng/mL | 0.16 pg/mL | [116] |
| AuNP/GQDs-PEI-GO | PSA | 0.001–100 ng/mL | 0.44 pg/mL | [114] |
| GQDs/AuNPs-ssDNA | p53 ssDNA | 25–400 nM | 13 nM | [118] |
| GQDs@AuNP | Carcinoembryonic antigen (CEA) | 0.1 pg/mL –10 ng/mL | 3.78 fg/mL | [119] |
| MoS$_2$-GQDs | DNA | 0.1 fM–1 nM | 0.025 fM | [120] |

## 6. SERS-Based Biosensing Applications of GQD Nanocomposites

SERS is a highly sensitive technique which is used to detect molecules with low concentrations. SERS is also a powerful tool with which to perform biological analysis of, for example, DNA, RNA, protein, blood, viruses and diseases [121]. The SERS technique can significantly enhance the weak intensity of the conventional Raman analysis, enabling

single molecule detection with high sensitivity and providing a specific fingerprint using a non-destructive method. Generally, the mechanisms of SERS are classified into two main principles, including electromagnetic enhancement (EM) and chemical enhancement (CM). The former is induced with the localized surface plasmon resonance (LSPR) of metallic nanoparticles, while the latter is promoted with the charge transfer between the substrate and adsorbed molecule. EM can provide significant enhancement in the order of $10^{10}$–$10^{11}$ [122], but the use of cost-inefficient noble metals (e.g., AgNPs and AuNPs) and the tendency for local Joule heating limit its usage, particularly in biological systems [123].

Therefore, much attention has been paid to the development of a noble-metal-free SERS substrate. A recent review article summarized the strategies for improving the SERS performance of noble-metal-free SERS materials [124]. GQDs as carbon-based nanomaterials emerge as a suitable candidate for SERS-based biosensing applications due to their inherent large conjugated π-domain, enabling high adsorption of biological compounds via a π–π interaction. Moreover, the plausibility of tuning the band structure of GQDs also allows one to freely adjust the CM for the desired biosensing application. As a result, many studies have reported GQD-based SERS on rhodamine B (RhB), rhodamine 6G (R6G), melamine and duphaston [125–128]. It is important to note that both CM and EM are not mutually exclusive; thus, GQDs and metallic NPs can be utilized together in a nanocomposite system to create more hot-spot sites through enhanced molecule adsorption via π–π stacking [83,89,129].

Zou et al. demonstrated a proof-of-concept experiment to generate a SERS sensor and fluorescence imaging platform for tuberculosis antigen (CFP-10) detection based on $Fe_3O_4$-Au-GQDs nanocomposites [117]. In a sandwich-type immunoassay using dual-mode nanoprobes, the GQDs acted as an excellent biolabeling material for simultaneous Raman scattering and PL, whereas the magneto-plasmonic (MagPlas) NPs simplified the immunoassay process and allowed fast and enhanced signal transduction. By immobilizing the MagPlas NPs and GQDs with a gold-binding protein fused with a monoclonal CFP-10 antibody (GBP-G2) and another monoclonal CFP-10 antibody (G3), a SERS-based immunosensor against CFP-10 antigen could be established. Figure 12a depicts the proportional Raman signal enhancement with an increasing concentration of the CFP-10 antigen. A linear correlation between the logarithmic CFP-10 antigen concentration versus Raman peak intensities at 1579 cm$^{-1}$ was obtained within the range of 1 pg/mL–1 μg/mL with an LoD of 0.05 pg/mL (Figure 12b).

As has been mentioned previously, Miao et al. fabricated Au-NGQD nanocomposites for SERS-based detection [85]. However, the formed nanocomposites were further conjugated with 4-nitrobenzenethiol (4-NBT) as the reporter and 4-mercaptophenylboronic acid (MPBA) as the targeting element to yield MPBA/4-NBT@Au-NGQD probes to specifically recognize glycan-overexpressed cancer cells via SERS imaging on a cell surface, as illustrated in Figure 12c. Sialic acid (SA), which is one of the glycans expressed on the cell membrane and is considered a potential cancer biomarker, was chosen as the model for the authors' study. For instance, according to the studies conducted by Baxi et al. [130] and Raval et al. [131], the total SA concentration in healthy people is approximately 44.62–47 mg/dL, while the SA concentration can reach up to 52.28 and 63.20 mg/dL for oral precancerous and oral cancer patients, respectively. On the other hand, another study revealed that patients with positive breast cancer had an SA concentration cutoff of >7 mg/dL [132]. The specific binding of MPBA to C-8,9 diol of glycans could occur at pH 7.4 through strong esterification, allowing one to profile glycan expression levels on the cell membrane after cell incubation with MPBA/4-NBT@Au-NGQD probes. The authors further validated their proposed strategy by using their probes for Raman profiling of SA expression levels in various cell lines, including MCF-7 (human breast cancer cell), HeLa (human epithelial cervical cancer cell) and L02 (normal liver cell) cells. Figure 12d displays the Raman images of the SA distribution on cell surfaces. The results demonstrated that higher SA expressions were found in MCF-7 and HeLa cells compared to L02 cells

(SA-negative normal cells), suggesting the feasibility of MPBA/4-NBT@Au-NGQD probes for the discrimination of SA-overexpressing cancer cells [85].

Jin et al. recently reported an interesting study about a noble metal/carbon nanozymatic SERS substrate using core-shell Ag/oxidized GQDs (Ag/o-GQDs) nanocomposites, bearing great potential for SERS bioanalysis at the subcellular level (Figure 12e) [84]. $H_2O_2$ is one of the major intracellular reactive oxygen species in tumor cells which can be monitored to understand the physiological cell response and efficacy of tumor therapy. The produced Ag/o-GQDs nanocomposites exhibited increasing and broadening plasmon adsorption and unique edge state charge transfer (CT) resonance in the long-wavelength of the visible light region (633 nm), promoting superior SERS sensitivity due to an enhanced EM effect and CT ability. In the proposed strategy, Ag/o-GQDs catalyzed the oxidation of TMB molecules in the presence of $H_2O_2$ and the SERS spectra of oxidized TMB were measured with 633 nm laser excitation. Therefore, the SERS intensity of oxidized TMB was strongly correlated with the concentration of $H_2O_2$, generating a linear relationship in the range of 30 nM–3 mM with an LoD of 4.22 nM. The formed nanocomposites were also demonstrated to be able to monitor $H_2O_2$ in human breast cancer cell MCF-7 in vitro.

Our group recently reported the fabrication of NGQD/AuNP nanocomposite sponges for multifunctional water treatment applications [87]. In our study, we showed that the nanocomposite sponges possessed stable solid-state PL which could be exploited for $Hg^{2+}$ sensing. Coupled with the presence of AuNPs in the nanocomposite as catalytic and SERS-active materials, our fabricated NGQD/AuNP sponges have great potential for PL-, catalytic-, and SERS-based biomolecules detection.

## 7. Conclusions and Perspectives

Since the last decade, many studies have been conducted on the synthesis, application, and fundamental aspects of GQDs to explore their potential across many fields. The development of a more environmentally friendly and controllable synthesis using earth-bound natural resources is a hot topic for materials scientists. In addition, the huge variety of functionalization techniques and outcomes make GQDs amenable for a broad application scope, especially for luminescence- and SERS-based biosensing. Moreover, integrating GQDs with either organic or inorganic materials to produce GQD-based nanocomposites can be considered one of the best strategies not only to achieve better sensing performance, but also to allow the detection of various analytes, even in a complicated biological system.

Nonetheless, the current understanding of the luminescence properties of GQDs and the possibility of synthesizing GQDs with uniform structures is still lacking. Different synthesis methods can yield GQDs with completely different structures, even using the same precursors. As a consequence, there are some discrepancies in the possible applications and mechanisms in the existing literature. Although density functional theory (DFT) calculations can provide vast additional insight into the fundamental aspects of GQDs, the obtained results still need to be proved or supported by experimental data, which are lacking. The already unclear understanding of GQDs is further complicated by the evolution of GQDs into nanocomposites, which adds more degrees of freedom to the system. On the other hand, the combination of CM, EM, charge transfer and improved hot-spot creation have facilitated SERS-based bio-detection, even in a complicated biological system. The practicality in real applications, however, is challenged, particularly by the precise control of the hot-spot locations in the substrates. Moreover, despite showing promise in SERS-based biological cell monitoring, the huge amount of data from the complex biological systems will make the data analysis process tedious and prone to human error. Thus, an association with artificial intelligence like big data analysis and machine learning should be expected in the future to successfully realize GQD nanocomposites not only as SERS-based, but also as luminescence-based biosensors.

The aforementioned issues make GQDs interesting and solving them will require researchers and scientists across many disciplines to contribute their expertise and collaborate with each other in order to bring to light the mysteries and overcome the challenges

related to GQDs and GQD nanocomposites, and to surpass the current knowledge in the biosensing field.

## References

1. Kroto, H.W.; Heath, J.R.; O'Brien, S.C.; Curl, R.F.; Smalley, R.E. C60: Buckminsterfullerene. *Nature* **1985**, *318*, 162–163. [CrossRef]
2. Iijima, S. Helical Microtubules of Graphitic Carbon. *Nature* **1991**, *354*, 56–58. [CrossRef]
3. Novoselov, K.S.; Geim, A.K.; Morozov, S.V.; Jiang, D.; Zhang, Y.; Dubonos, S.V.; Grigorieva, I.V.; Firsov, A.A. Electric Field Effect in Atomically Thin Carbon Films. *Science* **2004**, *306*, 666–669. [CrossRef] [PubMed]
4. Novoselov, K.S.; Jiang, Z.; Zhang, Y.; Morozov, S.V.; Stormer, H.L.; Zeitler, U.; Maan, J.C.; Boebinger, G.S.; Kim, P.; Geim, A.K. Room-Temperature Quantum Hall Effect in Graphene. *Science* **2007**, *315*, 1379. [CrossRef]
5. Ponomarenko, L.A.; Schedin, F.; Katsnelson, M.I.; Yang, R.; Hill, E.W.; Novoselov, K.S.; Geim, A.K. Chaotic Dirac Billiard in Graphene Quantum Dots. *Science* **2008**, *320*, 356–358. [CrossRef]
6. Pan, D.; Zhang, J.; Li, Z.; Wu, M. Hydrothermal Route for Cutting Graphene Sheets into Blue-Luminescent Graphene Quantum Dots. *Adv. Mater.* **2010**, *22*, 734–738. [CrossRef]
7. Sk, M.A.; Ananthanarayanan, A.; Huang, L.; Lim, K.H.; Chen, P. Revealing the Tunable Photoluminescence Properties of Graphene Quantum Dots. *J. Mater. Chem. C* **2014**, *2*, 6954–6960. [CrossRef]
8. Li, M.; Chen, T.; Gooding, J.J.; Liu, J. Review of Carbon and Graphene Quantum Dots for Sensing. *ACS Sens.* **2019**, *4*, 1732–1748. [CrossRef]
9. Sohal, N.; Maity, B.; Basu, S. Recent Advances in Heteroatom-Doped Graphene Quantum Dots for Sensing Applications. *RSC Adv.* **2021**, *11*, 25586–25615. [CrossRef]
10. Revesz, I.A.; Hickey, S.M.; Sweetman, M.J. Metal Ion Sensing with Graphene Quantum Dots: Detection of Harmful Contaminants and Biorelevant Species. *J. Mater. Chem. B* **2022**, *10*, 4346–4362. [CrossRef]
11. Lu, H.; Li, W.; Dong, H.; Wei, M. Graphene Quantum Dots for Optical Bioimaging. *Small* **2019**, *15*, e1902136. [CrossRef] [PubMed]
12. Chung, S.; Revia, R.A.; Zhang, M. Graphene Quantum Dots and Their Applications in Bioimaging, Biosensing, and Therapy. *Adv. Mater.* **2021**, *33*, e1904362. [CrossRef] [PubMed]
13. Khodadadei, F.; Safarian, S.; Ghanbari, N. Methotrexate-Loaded Nitrogen-Doped Graphene Quantum Dots Nanocarriers as an Efficient Anticancer Drug Delivery System. *Mater. Sci. Eng. C* **2017**, *79*, 280–285. [CrossRef] [PubMed]
14. Cheng, C.; Liang, Q.; Yan, M.; Liu, Z.; He, Q.; Wu, T.; Luo, S.; Pan, Y.; Zhao, C.; Liu, Y. Advances in Preparation, Mechanism and Applications of Graphene Quantum Dots/Semiconductor Composite Photocatalysts: A Review. *J. Hazard. Mater.* **2022**, *424 Pt D*, 127721. [CrossRef]
15. Son, D.I.; Kwon, B.W.; Park, D.H.; Seo, W.S.; Yi, Y.; Angadi, B.; Lee, C.-L.; Choi, W.K. Emissive ZnO-Graphene Quantum Dots for White-Light-Emitting Diodes. *Nat. Nanotechnol.* **2012**, *7*, 465–471. [CrossRef] [PubMed]
16. Li, X.; Rui, M.; Song, J.; Shen, Z.; Zeng, H. Carbon and Graphene Quantum Dots for Optoelectronic and Energy Devices: A Review. *Adv. Funct. Mater.* **2015**, *25*, 4929–4947. [CrossRef]
17. Kim, D.H.; Kim, T.W. Ultrahigh Current Efficiency of Light-Emitting Devices Based on Octadecylamine-Graphene Quantum Dots. *Nano Energy* **2017**, *32*, 441–447. [CrossRef]
18. Ghosh, D.; Sarkar, K.; Devi, P.; Kim, K.-H.; Kumar, P. Current and Future Perspectives of Carbon and Graphene Quantum Dots: From Synthesis to Strategy for Building Optoelectronic and Energy Devices. *Renew. Sustain. Energy Rev.* **2021**, *135*, 110391. [CrossRef]
19. Tsai, H.; Shrestha, S.; Vilá, R.A.; Huang, W.; Liu, C.; Hou, C.-H.; Huang, H.-H.; Wen, X.; Li, M.; Wiederrecht, G.; et al. Bright and Stable Light-Emitting Diodes Made with Perovskite Nanocrystals Stabilized in Metal–Organic Frameworks. *Nat. Photon.* **2021**, *15*, 843–849. [CrossRef]

20. Ren, X.; Zhang, X.; Xie, H.; Cai, J.; Wang, C.; Chen, E.; Xu, S.; Ye, Y.; Sun, J.; Yan, Q.; et al. Perovskite Quantum Dots for Emerging Displays: Recent Progress and Perspectives. *Nanomaterials* **2022**, *12*, 2243. [CrossRef]

21. Thoniyot, P.; Tan, M.J.; Karim, A.A.; Young, D.J.; Loh, X.J. Nanoparticle-Hydrogel Composites: Concept, Design, and Applications of These Promising, Multi-Functional Materials. *Adv. Sci.* **2015**, *2*, 1400010. [CrossRef] [PubMed]

22. Wang, J.; Koo, K.M.; Wang, Y.; Trau, M. Engineering State-of-the-Art Plasmonic Nanomaterials for SERS-Based Clinical Liquid Biopsy Applications. *Adv. Sci.* **2019**, *6*, 1900730. [CrossRef] [PubMed]

23. Yan, Y.; Gong, J.; Chen, J.; Zeng, Z.; Huang, W.; Pu, K.; Liu, J.; Chen, P. Recent Advances on Graphene Quantum Dots: From Chemistry and Physics to Applications. *Adv. Mater.* **2019**, *31*, e1808283. [CrossRef] [PubMed]

24. Li, L.; Wu, G.; Yang, G.; Peng, J.; Zhao, J.; Zhu, J.-J. Focusing on Luminescent Graphene Quantum Dots: Current Status and Future Perspectives. *Nanoscale* **2013**, *5*, 4015–4039. [CrossRef]

25. Zheng, X.T.; Ananthanarayanan, A.; Luo, K.Q.; Chen, P. Glowing Graphene Quantum Dots and Carbon Dots: Properties, Syntheses, and Biological Applications. *Small* **2015**, *11*, 1620–1636. [CrossRef]

26. Xu, Q.; Zhou, Q.; Hua, Z.; Xue, Q.; Zhang, C.; Wang, X.; Pan, D.; Xiao, M. Single-Particle Spectroscopic Measurements of Fluorescent Graphene Quantum Dots. *ACS Nano* **2013**, *7*, 10654–10661. [CrossRef]

27. Kim, S.; Hwang, S.W.; Kim, M.-K.; Shin, D.Y.; Shin, D.H.; Kim, C.O.; Yang, S.B.; Park, J.H.; Hwang, E.; Choi, S.-H.; et al. Anomalous Behaviors of Visible Luminescence from Graphene Quantum Dots: Interplay between Size and Shape. *ACS Nano* **2012**, *6*, 8203–8208. [CrossRef]

28. Jin, S.H.; Kim, D.H.; Jun, G.H.; Hong, S.H.; Jeon, S. Tuning the Photoluminescence of Graphene Quantum Dots through the Charge Transfer Effect of Functional Groups. *ACS Nano* **2013**, *7*, 1239–1245. [CrossRef]

29. Dai, Y.; Long, H.; Wang, X.; Wang, Y.; Gu, Q.; Jiang, W.; Wang, Y.; Li, C.; Zeng, T.H.; Sun, Y.; et al. Versatile Graphene Quantum Dots with Tunable Nitrogen Doping. *Part. Part. Syst. Charact.* **2014**, *31*, 597–604. [CrossRef]

30. Ju, J.; Chen, W. Synthesis of Highly Fluorescent Nitrogen-Doped Graphene Quantum Dots for Sensitive, Label-Free Detection of Fe (III) in Aqueous Media. *Biosens. Bioelectron.* **2014**, *58*, 219–225. [CrossRef]

31. Kurniawan, D.; Chiang, W.-H. Microplasma-Enabled Colloidal Nitrogen-Doped Graphene Quantum Dots for Broad-Range Fluorescent pH Sensors. *Carbon* **2020**, *167*, 675–684. [CrossRef]

32. Zhu, C.; Yang, S.; Wang, G.; Mo, R.; He, P.; Sun, J.; Di, Z.; Yuan, N.; Ding, J.; Ding, G.; et al. Negative Induction Effect of Graphite N on Graphene Quantum Dots: Tunable Band Gap Photoluminescence. *J. Mater. Chem. C* **2015**, *3*, 8810–8816. [CrossRef]

33. Noor, N.F.M.; Badri, M.A.S.; Salleh, M.M.; Umar, A.A. Synthesis of White Fluorescent Pyrrolic Nitrogen-Doped Graphene Quantum Dots. *Opt. Mater.* **2018**, *83*, 306–314. [CrossRef]

34. Yeh, T.-F.; Teng, C.-Y.; Chen, S.-J.; Teng, H. Nitrogen-Doped Graphene Oxide Quantum Dots as Photocatalysts for Overall Water-Splitting under Visible Light Illumination. *Adv. Mater.* **2014**, *26*, 3297–3303. [CrossRef] [PubMed]

35. Du, Y.; Guo, S. Chemically Doped Fluorescent Carbon and Graphene Quantum Dots for Bioimaging, Sensor, Catalytic and Photoelectronic Applications. *Nanoscale* **2016**, *8*, 2532–2543. [CrossRef] [PubMed]

36. Park, Y.; Yoo, J.; Lim, B.; Kwon, W.; Rhee, S.-W. Improving the Functionality of Carbon Nanodots: Doping and Surface Functionalization. *J. Mater. Chem. A* **2016**, *4*, 11582–11603. [CrossRef]

37. Chong, Y.; Ma, Y.; Shen, H.; Tu, X.; Zhou, X.; Xu, J.; Dai, J.; Fan, S.; Zhang, Z. The In Vitro and In Vivo Toxicity of Graphene Quantum Dots. *Biomaterials* **2014**, *35*, 5041–5048. [CrossRef]

38. Shang, W.; Zhang, X.; Zhang, M.; Fan, Z.; Sun, Y.; Han, M.; Fan, L. The Uptake Mechanism and Biocompatibility of Graphene Quantum Dots with Human Neural Stem Cells. *Nanoscale* **2014**, *6*, 5799–5806. [CrossRef]

39. Wang, S.; Cole, I.S.; Li, Q. The Toxicity of Graphene Quantum Dots. *RSC Adv.* **2016**, *6*, 89867–89878. [CrossRef]

40. Henna, T.K.; Pramod, K. Graphene Quantum Dots Redefine Nanobiomedicine. *Mater. Sci. Eng. C Mater. Biol. Appl.* **2020**, *110*, 110651. [CrossRef]

41. Liang, L.; Peng, X.; Sun, F.; Kong, Z.; Shen, J.-W. A Review on the Cytotoxicity of Graphene Quantum Dots: From Experiment to Simulation. *Nanoscale Adv.* **2021**, *3*, 904–917. [CrossRef] [PubMed]

42. Ye, R.; Xiang, C.; Lin, J.; Peng, Z.; Huang, K.; Yan, Z.; Cook, N.P.; Samuel, E.L.; Hwang, C.-C.; Ruan, G.; et al. Coal as an Abundant Source of Graphene Quantum Dots. *Nat. Commun.* **2013**, *4*, 2943. [CrossRef] [PubMed]

43. Zhang, Y.; Li, K.; Ren, S.; Dang, Y.; Liu, G.; Zhang, R.; Zhang, K.; Long, X.; Jia, K. Coal-Derived Graphene Quantum Dots Produced by Ultrasonic Physical Tailoring and Their Capacity for Cu(II) Detection. *ACS Sustain. Chem. Eng.* **2019**, *7*, 9793–9799. [CrossRef]

44. He, M.; Guo, X.; Huang, J.; Shen, H.; Zeng, Q.; Wang, L. Mass Production of Tunable Multicolor Graphene Quantum Dots from an Energy Resource of Coke By a One-Step Electrochemical Exfoliation. *Carbon* **2018**, *140*, 508–520. [CrossRef]

45. Liu, B.; Xie, J.; Ma, H.; Zhang, X.; Pan, Y.; Lv, J.; Ge, H.; Ren, N.; Su, H.; Xie, X.; et al. From Graphite to Graphene Oxide and Graphene Oxide Quantum Dots. *Small* **2017**, *13*, 1601001. [CrossRef]

46. Shinde, D.B.; Pillai, V.K. Electrochemical Preparation of Luminescent Graphene Quantum Dots from Multiwalled Carbon Nanotubes. *Chem. Eur. J.* **2012**, *18*, 12522–12528. [CrossRef]

47. Shin, Y.; Park, J.; Hyun, D.; Yang, J.; Lee, J.-H.; Kim, J.-H.; Lee, H. Acid-Free and Oxone Oxidant-Assisted Solvothermal Synthesis of Graphene Quantum Dots Using Various Natural Carbon Materials as Resources. *Nanoscale* **2015**, *7*, 5633–5637. [CrossRef]

48. Peng, J.; Gao, W.; Gupta, B.K.; Liu, Z.; Romero-Aburto, R.; Ge, L.; Song, L.; Alemany, L.B.; Zhan, X.; Gao, G.; et al. Graphene Quantum Dots Derived from Carbon Fibers. *Nano Lett.* **2012**, *12*, 844–849. [CrossRef]

49. Wang, L.; Wang, Y.; Xu, T.; Liao, H.; Yao, C.; Liu, Y.; Li, Z.; Chen, Z.; Pan, D.; Sun, L.; et al. Gram-Scale Synthesis of Single-Crystalline Graphene Quantum Dots with Superior Optical Properties. *Nat. Commun.* **2014**, *5*, 5357. [CrossRef]

50. Shen, C.; Ge, S.; Pang, Y.; Xi, F.; Liu, J.; Dong, X.; Chen, P. Facile and Scalable Preparation of Highly Luminescent N,S Co-Doped Graphene Quantum Dots and Their Application for Parallel Detection of Multiple Metal Ions. *J. Mater. Chem. B* **2017**, *5*, 6593–6600. [CrossRef]

51. Abbas, A.; Mariana, L.T.; Phan, A.N. Biomass-Waste Derived Graphene Quantum Dots and Their Applications. *Carbon* **2018**, *140*, 77–99. [CrossRef]

52. Dong, Y.; Shao, J.; Chen, C.; Li, H.; Wang, R.; Chi, Y.; Lin, X.; Chen, G. Blue Luminescent Graphene Quantum Dots and Graphene Oxide Prepared By Tuning the Carbonization Degree of Citric Acid. *Carbon* **2012**, *50*, 4738–4743. [CrossRef]

53. Tang, L.; Ji, R.; Cao, X.; Lin, J.; Jiang, H.; Li, X.; Teng, K.S.; Luk, C.M.; Zeng, S.; Hao, J.; et al. Deep Ultraviolet Photoluminescence of Water-Soluble Self-Passivated Graphene Quantum Dots. *ACS Nano* **2012**, *6*, 5102–5110. [CrossRef] [PubMed]

54. Ding, Z.; Li, F.; Wen, J.; Wang, X.; Sun, R. Gram-Scale Synthesis of Single-Crystalline Graphene Quantum Dots Derived from Lignin Biomass. *Green Chem.* **2018**, *20*, 1383–1390. [CrossRef]

55. Kumar, S.; Aziz, S.K.T.; Girshevitz, O.; Nessim, G.D. One-Step Synthesis of N-Doped Graphene Quantum Dots from Chitosan as a Sole Precursor Using Chemical Vapor Deposition. *J. Phys. Chem. C* **2018**, *122*, 2343–2349. [CrossRef]

56. Sankaran, R.M.; Giapis, K.P. Hollow Cathode Sustained Plasma Microjets: Characterization and Application to Diamond Deposition. *J. Appl. Phys.* **2002**, *92*, 2406–2411. [CrossRef]

57. Kurniawan, D.; Weng, R.-J.; Setiawan, O.; Ostrikov, K.K.; Chiang, W.-H. Microplasma Nanoengineering of Emission-Tuneable Colloidal Nitrogen-Doped Graphene Quantum Dots as Smart Environmental-Responsive Nanosensors and Nanothermometers. *Carbon* **2021**, *185*, 501–513. [CrossRef]

58. Lu, Y.; Xu, S.F.; Zhong, X.X.; Ostrikov, K.; Cvelbar, U.; Mariotti, D. Characterization of a DC-Driven Microplasma between a Capillary Tube and Water Surface. *EPL* **2013**, *102*, 15002. [CrossRef]

59. Bruggeman, P.J.; Kushner, M.J.; Locke, B.R.; Gardeniers, J.G.E.; Graham, W.G.; Graves, D.B.; Hofman-Caris, R.C.H.M.; Maric, D.; Reid, J.P.; Ceriani, E.; et al. Plasma–Liquid Interactions: A Review and Roadmap. *Plasma Sources Sci. Technol.* **2016**, *25*, 053002. [CrossRef]

60. Zhou, R.; Zhou, R.; Prasad, K.; Fang, Z.; Speight, R.; Bazaka, K.; Ostrikov, K.K. Cold Atmospheric Plasma Activated Water as a Prospective Disinfectant: The Crucial Role of Peroxynitrite. *Green Chem.* **2018**, *20*, 5276–5284. [CrossRef]

61. Park, S.; Park, J.Y.; Choe, W. Origin of Hydroxyl Radicals in a Weakly Ionized Plasma-Facing Liquid. *Chem. Eng. J.* **2019**, *378*, 122163. [CrossRef]

62. Wang, Z.; Lu, Y.; Yuan, H.; Ren, Z.; Xu, C.; Chen, J. Microplasma-Assisted Rapid Synthesis of Luminescent Nitrogen-Doped Carbon Dots and Their Application in pH Sensing and Uranium Detection. *Nanoscale* **2015**, *7*, 20743–20748. [CrossRef] [PubMed]

63. Chiang, W.-H.; Richmonds, C.; Sankaran, R.M. Continuous-Flow, Atmospheric-Pressure Microplasmas: A Versatile Source for Metal Nanoparticle Synthesis in the Gas or Liquid Phase. *Plasma Sources Sci. Technol.* **2010**, *19*, 034011. [CrossRef]

64. Weerasinghe, J.; Scott, J.; Deshan, A.D.K.; Chen, D.; Singh, A.; Sen, S.; Sonar, P.; Vasilev, K.; Li, Q.; Ostrikov, K.K. Monochromatic Blue and Switchable Blue-Green Carbon Quantum Dots by Room-Temperature Air Plasma Processing. *Adv. Mater. Technol.* **2021**, *7*, 2100586. [CrossRef]

65. Chang, G.-Y.; Kurniawan, D.; Chang, Y.-J.; Chiang, W.-H. Microplasma-Enabled Surfaced-Functionalized Silicon Quantum Dots for Label-Free Detection of Dopamine. *ACS Omega* **2022**, *7*, 223–229. [CrossRef]

66. Kurniawan, D.; Jhang, R.-C.; Ostrikov, K.K.; Chiang, W.-H. Microplasma-Tunable Graphene Quantum Dots for Ultrasensitive and Selective Detection of Cancer and Neurotransmitter Biomarkers. *ACS Appl. Mater. Interfaces* **2021**, *13*, 34572–34583. [CrossRef]

67. Kurniawan, D.; Anjali, B.A.; Setiawan, O.; Ostrikov, K.K.; Chung, Y.G.; Chiang, W.-H. Microplasma Band Structure Engineering in Graphene Quantum Dots for Sensitive and Wide-Range pH Sensing. *ACS Appl. Mater. Interfaces* **2022**, *14*, 1670–1683. [CrossRef]

68. Yeh, P.-C.; Yoon, S.; Kurniawan, D.; Chung, Y.G.; Chiang, W.-H. Unraveling the Fluorescence Quenching of Colloidal Graphene Quantum Dots for Selective Metal Ion Detection. *ACS Appl. Nano Mater.* **2021**, *4*, 5636–5642. [CrossRef]

69. Kurniawan, D.; Sharma, N.; Rahardja, M.R.; Cheng, Y.-Y.; Chen, Y.-T.; Wu, G.-X.; Yeh, Y.-Y.; Yeh, P.-C.; Ostrikov, K.K.; Chiang, W.-H. Plasma Nanoengineering of Bioresource-Derived Graphene Quantum Dots as Ultrasensitive Environmental Nanoprobes. *ACS Appl. Mater. Interfaces* **2022**. [CrossRef]

70. Yang, J.-S.; Pai, D.Z.; Chiang, W.-H. Microplasma-Enhanced Synthesis of Colloidal Graphene Quantum Dots at Ambient Conditions. *Carbon* **2019**, *153*, 315–319. [CrossRef]

71. Orriere, T.; Kurniawan, D.; Chang, Y.-C.; Pai, D.Z.; Chiang, W.-H. Effect of Plasma Polarity on the Synthesis of Graphene Quantum Dots by Atmospheric-Pressure Microplasmas. *Nanotechnology* **2020**, *31*, 485001. [CrossRef] [PubMed]

72. Sun, P.P.; Araud, E.M.; Huang, C.; Shen, Y.; Monroy, G.L.; Zhong, S.; Tong, Z.; Boppart, S.A.; Eden, J.G.; Nguyen, T.H. Disintegration of Simulated Drinking Water Biofilms with Arrays of Microchannel Plasma Jets. *NPJ Biofilms Microbiomes* **2018**, *4*, 24. [CrossRef] [PubMed]

73. Chiang, W.-H.; Mariotti, D.; Sankaran, R.M.; Eden, J.G.; Ostrikov, K.K. Microplasmas for Advanced Materials and Devices. *Adv. Mater.* **2020**, *32*, e1905508. [CrossRef] [PubMed]

74. Lin, L.; Pho, H.Q.; Zong, L.; Li, S.; Pourali, N.; Rebrov, E.; Tran, N.N.; Ostrikov, K.K.; Hessel, V. Microfluidic Plasmas: Novel Technique for Chemistry and Chemical Engineering. *Chem. Eng. J.* **2021**, *417*, 129355. [CrossRef]

75. Mousavi, S.M.; Hashemi, S.A.; Kalashgrani, M.Y.; Omidifar, N.; Bahrani, S.; Rao, N.V.; Babapoor, A.; Gholami, A.; Chiang, W.-H. Bioactive Graphene Quantum Dots Based Polymer Composite for Biomedical Applications. *Polymers* **2022**, *14*, 617. [CrossRef]

76. Kovalchuk, A.; Huang, K.; Xiang, C.; Marti, A.A.; Tour, J.M. Luminescent Polymer Composite Films Containing Coal-Derived Graphene Quantum Dots. *ACS Appl. Mater. Interfaces* **2015**, *7*, 26063–26068. [CrossRef]

77. Chen, Y.-X.; Lu, D.; Wang, G.-G.; Huangfu, J.; Wu, Q.-B.; Wang, X.-F.; Liu, L.-F.; Ye, D.-M.; Yan, B.; Han, J. Highly Efficient Orange Emissive Graphene Quantum Dots Prepared by Acid-Free Method for White LEDs. *ACS Sustain. Chem. Eng.* **2020**, *8*, 6657–6666. [CrossRef]

78. Nair, R.V.; Thomas, R.T.; Mohamed, A.P.; Pillai, S. Fluorescent Turn-Off Sensor Based on Sulphur-Doped Graphene Quantum Dots in Colloidal and Film Forms for the Ultrasensitive Detection of Carbamate Pesticides. *Microchem. J.* **2020**, *157*, 104971. [CrossRef]

79. Liu, M. Optical Properties of Carbon Dots: A Review. *Nanoarchitectonics* **2019**, *1*, 1–12. [CrossRef]

80. Laysandra, L.; Chuang, C.-H.; Kobayashi, S.; Au-Duong, A.-N.; Cheng, Y.-H.; Li, Y.-T.; Mburu, M.M.; Isono, T.; Satoh, T.; Chiu, Y.-C. Design of Self-Cross-Linkable Poly(n-butyl acrylate)-co-poly[N-(hydroxymethyl)acrylamide] Amphiphilic Copolymers toward Elastic and Self-Healing Properties. *ACS Appl. Polym. Mater.* **2020**, *2*, 5432–5443. [CrossRef]

81. Laysandra, L.; Kurniawan, D.; Wang, C.-L.; Chiang, W.-H.; Chiu, Y.-C. Synergistic Effect in a Graphene Quantum Dot-Enabled Luminescent Skinlike Copolymer for Long-Term pH Detection. *ACS Appl. Mater. Interfaces* **2021**, *13*, 60413–60424. [CrossRef] [PubMed]

82. Li, Y.; Hu, Y.; Zhao, Y.; Shi, G.; Deng, L.; Hou, Y.; Qu, L. An Electrochemical Avenue to Green-Luminescent Graphene Quantum Dots as Potential Electron-Acceptors for Photovoltaics. *Adv. Mater.* **2011**, *23*, 776–780. [CrossRef] [PubMed]

83. Ge, J.; Li, Y.; Wang, J.; Pu, Y.; Xue, W.; Liu, X. Green Synthesis of Graphene Quantum Dots and Silver Nanoparticles Compounds with Excellent Surface Enhanced Raman Scattering Performance. *J. Alloys Compd.* **2016**, *663*, 166–171. [CrossRef]

84. Jin, J.; Song, W.; Wang, J.; Li, L.; Tian, Y.; Zhu, S.; Zhang, Y.; Xu, S.; Yang, B.; Zhao, B. A Highly Sensitive SERS Platform Based on Small-Sized Ag/GQDs Nanozyme for Intracellular Analysis. *Chem. Eng. J.* **2022**, *430*, 132687. [CrossRef]

85. Miao, X.; Wen, S.; Su, Y.; Fu, J.; Luo, X.; Wu, P.; Cai, C.; Jelinek, R.; Jiang, L.-P.; Zhu, J.-J. Graphene Quantum Dots Wrapped Gold Nanoparticles with Integrated Enhancement Mechanisms as Sensitive and Homogeneous Substrates for Surface-Enhanced Raman Spectroscopy. *Anal. Chem.* **2019**, *91*, 7295–7303. [CrossRef] [PubMed]

86. Das, R.; Paul, K.K.; Giri, P.K. Highly Sensitive and Selective Label-Free Detection of Dopamine in Human Serum Based on Nitrogen-Doped Graphene Quantum Dots Decorated on Au Nanoparticles: Mechanistic Insights Through Microscopic and Spectroscopic Studies. *Appl. Surf. Sci.* **2019**, *490*, 318–330. [CrossRef]

87. Kurniawan, D.; Rahardja, M.R.; Fedotov, P.V.; Obraztsova, E.D.; Ostrikov, K.K.; Chiang, W.-H. Plasma-Bioresource-Derived Multifunctional Porous NGQD/AuNP Nanocomposites for Water Monitoring and Purification. *Chem. Eng. J.* **2023**, *451*, 139083. [CrossRef]

88. Thakur, M.K.; Fang, C.-Y.; Yang, Y.-T.; Effendi, T.A.; Roy, P.K.; Chen, R.-S.; Ostrikov, K.K.; Chiang, W.-H.; Chattopadhyay, S. Microplasma-Enabled Graphene Quantum Dot-Wrapped Gold Nanoparticles with Synergistic Enhancement for Broad Band Photodetection. *ACS Appl. Mater. Interfaces* **2020**, *12*, 28550–28560. [CrossRef]

89. Wang, J.; Gao, X.; Sun, H.; Su, B.; Gao, C. Monodispersed Graphene Quantum Dots Encapsulated Ag Nanoparticles for Surface-Enhanced Raman Scattering. *Mater. Lett.* **2016**, *162*, 142–145. [CrossRef]

90. Liu, J.; Qin, L.; Kang, S.-Z.; Li, G.; Li, X. Gold Nanoparticles/Glycine Derivatives/Graphene Quantum Dots Composite with Tunable Fluorescence and Surface Enhanced Raman Scattering Signals for Cellular Imaging. *Mater. Des.* **2017**, *123*, 32–38. [CrossRef]

91. Sun, J.; Cui, F.; Zhang, R.; Gao, Z.; Ji, J.; Ren, Y.; Pi, F.; Zhang, Y.; Sun, X. Comet-like Heterodimers "Gold Nanoflower @Graphene Quantum Dots" Probe with FRET "Off" to DNA Circuit Signal "On" for Sensing and Imaging MicroRNA In Vitro and In Vivo. *Anal. Chem.* **2018**, *90*, 11538–11547. [CrossRef] [PubMed]

92. Zhang, R.; Sun, J.; Ji, J.; Pi, F.; Xiao, Y.; Zhang, Y.; Sun, X. A Novel "OFF-ON" Biosensor Based on Nanosurface Energy Transfer between Gold Nanocrosses and Graphene Quantum Dots for Intracellular ATP Sensing and Tracking. *Sens. Actuators B Chem.* **2019**, *282*, 910–916. [CrossRef]

93. Yan, X.; Zhao, X.-E.; Sun, J.; Zhu, S.; Lei, C.; Li, R.; Gong, P.; Ling, B.; Wang, R.; Wang, H. Probing Glutathione Reductase Activity with Graphene Quantum Dots and Gold Nanoparticles System. *Sens. Actuators B Chem.* **2018**, *263*, 27–35. [CrossRef]

94. Abdolmohammad-Zadeh, H.; Ahmadian, F. A Fluorescent Biosensor Based on Graphene Quantum Dots/Zirconium-Based Metal-Organic Framework Nanocomposite as a Peroxidase Mimic for Cholesterol Monitoring in Human Serum. *Microchem. J.* **2021**, *164*, 106001. [CrossRef]

95. He, Y.; Wang, X.; Sun, J.; Jiao, S.; Chen, H.; Gao, F.; Wang, L. Fluorescent Blood Glucose Monitor by Hemin-Functionalized Graphene Quantum Dots Based Sensing System. *Anal. Chim. Acta* **2014**, *810*, 71–78. [CrossRef] [PubMed]

96. Zhang, L.; Hai, X.; Xia, C.; Chen, X.-W.; Wang, J.-H. Growth of CuO Nanoneedles on Graphene Quantum Dots as Peroxidase Mimics for Sensitive Colorimetric Detection of Hydrogen Peroxide and Glucose. *Sens. Actuators B Chem.* **2017**, *248*, 374–384. [CrossRef]

97. Wang, H.; Liu, C.; Liu, Z.; Ren, J.; Qu, X. Specific Oxygenated Groups Enriched Graphene Quantum Dots as Highly Efficient Enzyme Mimics. *Small* **2018**, *14*, e1703710. [CrossRef] [PubMed]

98. Adel, R.; Ebrahim, S.; Shokry, A.; Soliman, M.; Khalil, M. Nanocomposite of CuInS/ZnS and Nitrogen-Doped Graphene Quantum Dots for Cholesterol Sensing. *ACS Omega* **2021**, *6*, 2167–2176. [CrossRef]

99. Kalkal, A.; Pradhan, R.; Kadian, S.; Manik, G.; Packirisamy, G. Biofunctionalized Graphene Quantum Dots Based Fluorescent Biosensor toward Efficient Detection of Small Cell Lung Cancer. *ACS Appl. Bio Mater.* **2020**, *3*, 4922–4932. [CrossRef]

100. Li, N.; Li, R.; Li, Z.; Yang, Y.; Wang, G.; Gu, Z. Pentaethylenehexamine and Histidine-Functionalized Graphene Quantum Dots for Ultrasensitive Fluorescence Detection of MicroRNA with Target and Molecular Beacon Double Cycle Amplification Strategy. *Sens. Actuators B Chem.* **2019**, *283*, 666–676. [CrossRef]

101. Sun, L.; Li, S.; Ding, W.; Yao, Y.; Yang, X.; Yao, C. Fluorescence Detection of Cholesterol Using a Nitrogen-Doped Graphene Quantum Dot/Chromium Picolinate Complex-Based Sensor. *J. Mater. Chem. B* **2017**, *5*, 9006–9014. [CrossRef] [PubMed]

102. Yang, P.; Zhu, Z.; Zhang, T.; Zhang, W.; Chen, W.; Cao, Y.; Chen, M.; Zhou, X. Orange-Emissive Carbon Quantum Dots: Toward Application in Wound pH Monitoring Based on Colorimetric and Fluorescent Changing. *Small* **2019**, *15*, 1902823. [CrossRef] [PubMed]

103. Schmid-Wendtner, M.-H.; Korting, H.C. The pH of the Skin Surface and Its Impact on the Barrier Function. *Skin Pharmacol. Physiol.* **2006**, *19*, 296–302. [CrossRef] [PubMed]

104. Baeyens, W.R.G.; Schulman, S.G.; Calokerinos, A.C.; Zhao, Y.; Campana, A.M.G.; Nakashima, K.; De Keukeleire, D. Chemiluminescence-Based Detection: Principles and Analytical Applications in Flowing Streams and in Immunoassays. *J. Pharm. Biomed. Anal.* **1998**, *17*, 941–953. [CrossRef] [PubMed]

105. Aboul-Enein, H.Y.; Stefan, R.-I.; van Staden, J.F. Chemiluminescence-Based (Bio)Sensors—An Overview. *Crit. Rev. Anal. Chem.* **1999**, *29*, 323–331. [CrossRef]

106. Lin, Z.; Chen, H.; Lin, J.-M. Peroxide Induced Ultra-Weak Chemiluminescence and Its Application in Analytical Chemistry. *Analyst* **2013**, *138*, 5182–5193. [CrossRef]

107. Mansuriya, B.D.; Altintas, Z. Applications of Graphene Quantum Dots in Biomedical Sensors. *Sensors* **2020**, *20*, 1072. [CrossRef]

108. Sun, Y.; Lin, Y.; Han, R.; Wang, X.; Luo, C. A Chemiluminescence Biosensor for Lysozyme Detection Based on Aptamers and Hemin/G-Quadruplex DNAzyme Modified Sandwich-Rod Carbon Fiber Composite. *Talanta* **2019**, *200*, 57–66. [CrossRef]

109. Shi, B.; Su, Y.; Duan, Y.; Chen, S.; Zuo, W. A Nanocomposite Prepared from Copper(II) and Nitrogen-Doped Graphene Quantum Dots with Peroxidase Mimicking Properties for Chemiluminescent Determination of Uric Acid. *Microchim. Acta* **2019**, *186*, 397. [CrossRef]

110. Hassanzadeh, J.; Khataee, A. Ultrasensitive Chemiluminescent Biosensor for the Detection of Cholesterol Based on Synergetic Peroxidase-Like Activity of $MoS_2$ and Graphene Quantum Dots. *Talanta* **2018**, *178*, 992–1000. [CrossRef]

111. Afsharipour, R.; Dadfarnia, S.; Shabani, A.M.H. Chemiluminescence Determination of Dopamine Using N, P-Graphene Quantum Dots after Preconcentration on Magnetic Oxidized Nanocellulose Modified with Graphene Quantum Dots. *Microchim. Acta* **2022**, *189*, 192. [CrossRef] [PubMed]

112. Richter, M.M. Electrochemiluminescence (ECL). *Chem. Rev.* **2004**, *104*, 3003–3036. [CrossRef] [PubMed]

113. Miao, W. Electrogenerated Chemiluminescence and Its Biorelated Applications. *Chem. Rev.* **2008**, *108*, 2506–2553. [CrossRef] [PubMed]

114. Yang, C.; Guo, Q.; Lu, Y.; Zhang, B.; Nie, G. Ultrasensitive "Signal-On" Electrochemiluminescence Immunosensor for Prostate-Specific Antigen Detection Based on Novel Nanoprobe and Poly(Indole-6-Carboxylic Acid)/Flower-Like Au Nanocomposite. *Sens. Actuators B Chem.* **2020**, *303*, 127246. [CrossRef]

115. Qin, D.; Jiang, X.; Mo, G.; Feng, J.; Yu, C.; Deng, B. A Novel Carbon Quantum Dots Signal Amplification Strategy Coupled with Sandwich Electrochemiluminescence Immunosensor for the Detection of CA15-3 in Human Serum. *ACS Sens.* **2019**, *4*, 504–512. [CrossRef] [PubMed]

116. Zuo, F.; Zhang, C.; Zhang, H.; Tan, X.; Chen, S.; Yuan, R. A Solid-State Electrochemiluminescence Biosensor for Con A Detection Based on CeO2@Ag Nanoparticles Modified Graphene Quantum Dots as Signal Probe. *Electrochim. Acta* **2019**, *294*, 76–83. [CrossRef]

117. Zou, F.; Zhou, H.; Tan, T.V.; Kim, J.; Koh, K.; Lee, J. Dual-Mode SERS-Fluorescence Immunoassay Using Graphene Quantum Dot Labeling on One-Dimensional Aligned Magnetoplasmonic Nanoparticles. *ACS Appl. Mater. Interfaces* **2015**, *7*, 12168–12175. [CrossRef]

118. Lu, Q.; Wei, W.; Zhou, Z.; Zhou, Z.; Zhang, Y.; Liu, S. Electrochemiluminescence Resonance Energy Transfer between Graphene Quantum Dots and Gold Nanoparticles for DNA Damage Detection. *Analyst* **2014**, *139*, 2404–2410. [CrossRef]

119. Nie, G.; Wang, Y.; Tang, Y.; Zhao, D.; Guo, Q. A Graphene Quantum Dots Based Electrochemiluminescence Immunosensor for Carcinoembryonic Antigen Detection Using Poly(5-Formylindole)/Reduced Graphene Oxide Nanocomposite. *Biosens. Bioelectron.* **2018**, *101*, 123–128. [CrossRef]

120. Sun, Y.; Huang, C.; Sun, X.; Wang, Q.; Zhao, P.; Ge, S.; Yu, J. Electrochemiluminescence Biosensor Based on Molybdenum Disulfide-Graphene Quantum Dots Nanocomposites and DNA Walker Signal Amplification for DNA Detection. *Microchim. Acta* **2021**, *188*, 353. [CrossRef]

121. Liang, X.; Li, N.; Zhang, R.; Yin, P.; Zhang, C.; Yang, N.; Liang, K.; Kong, B. Carbon-Based SERS Biosensor: From Substrate Design to Sensing and Bioapplication. *NPG Asia Mater.* **2021**, *13*, 8. [CrossRef]

122. Blackie, E.J.; Ru, E.C.L.; Etchegoin, P.G. Single-Molecule Surface-Enhanced Raman Spectroscopy of Nonresonant Molecules. *J. Am. Chem. Soc.* **2009**, *131*, 14466–14472. [CrossRef] [PubMed]

123. Li, D.; Aubertin, K.; Onidas, D.; Nizard, P.; Felidj, N.; Gazeau, F.; Mangeney, C.; Luo, Y. Recent Advances in Non-Plasmonic Surface-Enhanced Raman Spectroscopy Nanostructures for Biomedical Applications. *WIREs Nanomed. Nanobiotechnol.* **2022**, *14*, e1795. [CrossRef] [PubMed]

124. Wang, X.; Zhang, E.; Shi, H.; Tao, Y.; Ren, X. Semiconductor-Based Surface Enhanced Raman Scattering (SERS): From Active Materials to Performance Improvement. *Analyst* **2022**, *147*, 1257–1272. [CrossRef] [PubMed]

125. Das, R.; Parveen, S.; Bora, A.; Giri, P.K. Origin of High Photoluminescence Yield and High SERS Sensitivity of Nitrogen-Doped Graphene Quantum Dots. *Carbon* **2020**, *160*, 273–286. [CrossRef]

126. Chang, Y.C.; Chiang, W.-H. Noble Metal-Free Surface-Enhanced Raman Scattering Enhancement from Bandgap-Controlled Graphene Quantum Dots. *Part. Part. Syst. Charact.* **2021**, *38*, 2100128. [CrossRef]

127. Sharma, V.; Som, N.N.; Pillai, S.B.; Jha, P.K. Utilization of Doped GQDs for Ultrasensitive Detection of Catastrophic Melamine: A New SERS Platform. *Spectrochim. Acta Part A Mol. Biomol. Spectrosc.* **2020**, *224*, 117352. [CrossRef]

128. Mary, Y.S.; Mary, Y.S. Utilization of Doped/Undoped Graphene Quantum Dots for Ultrasensitive Detection of Duphaston, a SERS Platform. *Spectrochim. Acta Part A Mol. Biomol. Spectrosc.* **2021**, *244*, 118865. [CrossRef] [PubMed]

129. Pandit, S.; Kunwar, S.; Kulkarni, R.; Mandavka, R.; Lin, S.; Lee, J. Fabrication of Hybrid Pd@Ag Core-Shell and Fully Alloyed Bi-Metallic AgPd NPs and SERS Enhancement of Rhodamine 6G by a Unique Mixture Approach with Graphene Quantum Dots. *Appl. Surf. Sci.* **2021**, *548*, 149252. [CrossRef]

130. Baxi, B.R.; Patel, P.S.; Adhvaryu, S.G.; Dayal, P.K. Usefulness of Serum Glycoconjugates in Precancerous and Cancerous Diseases of the Oral Cavity. *Cancer* **1991**, *67*, 135–140. [CrossRef]

131. Raval, G.N.; Patel, D.D.; Parekh, L.J.; Patel, J.B.; Shah, M.H.; Patel, P.S. Evaluation of Serum Sialic Acid, Sialyltransferase and Sialoproteins in Oral Cavity Cancer. *Oral Dis.* **2003**, *9*, 119–128. [CrossRef] [PubMed]

132. Hernández-Arteaga, A.; Nava, J.D.J.Z.; Kolosovas-Machuca, E.S.; Velázquez-Salazar, J.J.; Vinogradova, E.; José-Yacamán, M.; Navarro-Contreras, H.R. Diagnosis of Breast Cancer by Analysis of Sialic Acid Concentrations in Human Saliva by Surface-Enhanced Raman Spectroscopy of Silver Nanoparticles. *Nano Res.* **2017**, *10*, 3662–3670. [CrossRef]